The Astrophysical Journal, 923:102 (20pp), 2021 December 10 https://doi.org/10.3847/1538-4357/ac22a6

Eta Carinae: A Tale of Two Periastron Passages

Theodore R. Gull[1], Felipe Navarete[2], Michael F. Corcoran[3,4], Augusto Damineli[2], David Espinoza[3], Kenji Hamaguchi[3,5], Henrik Hartman[6], D. John Hillier[7], Thomas Madura[8], Anthony F. J. Moffat[9,10], Patrick Morris[11], Krister Nielsen[4], Julian M. Pittard[12], Andrew M. T. Pollock[13], Noel D. Richardson[14], Christopher M. P. Russell[3,4], Ian R. Stevens[15], and Gerd Weigelt[16]

[1] Exoplanets and Stellar Astrophysics Laboratory, NASA/Goddard Space Flight Center, Greenbelt, MD 20771, USA; tedgull@gmail.com
[2] Universidade de São Paulo, IAG, Rua do Matão 1226, Cidade Universitária São Paulo-SP, 05508-090, Brasil
[3] CRESST and X-ray Astrophysics Laboratory, NASA/Goddard Space Flight Center, Greenbelt, MD 20771, USA
[4] The Catholic University of America, 620 Michigan Avenue N.E., Washington, DC 20064, USA
[5] Department of Physics, University of Maryland Baltimore County, 1000 Hilltop Circle, Baltimore, MD 21250, USA
[6] Materials Science and Applied Mathematics, Malmö University, SE-20506 Malmö, Sweden
[7] Department of Physics and Astronomy & Pittsburgh Particle Physics, Astrophysics, and Cosmology Center (PITT PACC), University of Pittsburgh, 3941 O'Hara Street, Pittsburgh, PA 15260, USA
[8] Department of Physics and Astronomy, San Jose State University, One Washington Square, San Jose, CA 95192, USA
[9] Département de physique, Université de Montréal, C.P. 6128, Succ. C-V, Montréal, QC H3C 3J7, Canada
[10] Centre de Recherche en Astrophysique du Québec, Canada
[11] California Institute of Technology, IPAC, M/C 100-22, Pasadena, CA 91125, USA
[12] School of Physics and Astronomy, The University of Leeds, Woodhouse Lane, Leeds, LS2 9JT, UK
[13] Department of Physics and Astronomy, University of Sheffield, Hounsfield Road, Sheffield S3 7RH, UK
[14] Department of Physics and Astronomy, Embry-Riddle Aeronautical University, 3700 Willow Creek Road, Prescott, AZ 86301, USA
[15] School of Physics & Astronomy, University of Birmingham, Birmingham B15 2TT, UK
[16] Max Planck Institute for Radio Astronomy, Auf dem Hügel 69, D-53121 Bonn, Germany
Received 2021 June 4; revised 2021 August 27; accepted 2021 August 30; published 2021 December 14

Abstract

Since 2002, the far-ultraviolet (FUV) flux (1150–1680 Å) of Eta Carinae, monitored by the Hubble Space Telescope/Space Telescope Imaging Spectrograph, has increased by an order of magnitude. This increase is attributed to partial dissipation of a line-of-sight (LOS) occulter that blocks the central core of the system. Across the 2020 February periastron passage, changes in the FUV emission show a stronger wavelength dependence than occurred across the 2003 July periastron passage. Across both periastron passages, most of the FUV spectrum dropped in flux then recovered a few months later. The 2020 periastron passage included enhancements of FUV flux in narrow spectral intervals near periastron followed by a transient absorption and recovery to pre-periastron flux levels. The drop in flux is due to increased absorption by singly ionized species as the secondary star plunges deep into the wind of the primary star, which blocks the companion's ionizing radiation. The enhanced FUV emission is caused by the companion's wind-blown cavity briefly opening a window to deeper layers of the primary star. This is the first time transient brightening has been seen in the FUV comparable to transients previously seen at longer wavelengths. Changes in resonance line-velocity profiles hint that the dissipating occulter is associated with material in LOS moving at −100 to −300 km s^{-1}, similar in velocity of structures previously associated with the 1890s lesser eruption.

Unified Astronomy Thesaurus concepts: Massive stars (732); Stellar winds (1636); Binary stars (154)

1. Introduction

Eta Carinae (η Car) has stimulated the curiosity of many astronomers for nearly two centuries since John Herschel and other observers noted variability in the 1820s. By late 1837, its apparent visual brightness had suddenly increased to rival Canopus and Sirius (Herschel 1838). In the 1840s, η Car reached a visible maximum close to that of Sirius, faded until a relatively minor brightening occurred in the 1890s, fading again until the 1940s, and has brightened continuously since then (Smith & Frew 2011; Damineli et al. 2019). The Homunculus (Gaviola 1950), today a $10'' \times 20''$ bipolar dusty shell, and the Little Homunculus, a $4'' \times 4''$ interior bipolar, ionized shell (Ishibashi et al. 2003), are the physical ejecta from outbursts associated with the two brightenings in the 19th century.

η Car is a unique massive binary system that underwent two major events, the very energetic Great Eruption in the 1840s and the Lesser Eruption in the 1890s, expelling massive amounts of ejecta ($\approx 40\,M_\odot$, Morris et al. 2017) and yet has survived as a binary with a primary ($\approx 100\,M_\odot$) and a hot secondary ($\approx 40\,M_\odot$). Whether the events were due to a near-supernova event or a merger from triple to binary (Portegies Zwart & van den Heuvel 2016; Hirai et al. 2021), we do not know, but gathering information about this dynamically changing system can only lead to new understanding of the evolution of massive stars in multiple stellar systems.

η Car was found to be a massive binary via the 5.54 yr, periodic spectroscopic appearances and disappearances of He I λ10830 and high excitation nebular lines (Damineli 1996; Damineli et al. 1997). Damineli et al. (1998) defined a long high-ionization state (appearance of [Ne III], [Fe III], [Ar III]) and a short low-ionization state ([Fe II]) associated with the periastron passage.

Pittard & Corcoran (2002) determined that the X-ray spectrum of η Car required that the massive primary wind ($V_{A\infty} \sim$ 500–700 km s^{-1}) must be colliding with a substantially faster secondary wind with $V_{B\infty} \sim 3000$ km s^{-1}. More recent models of the binary η Car have suggested that the primary (η Car-A) wind properties are $V_{A\infty} \sim 420$ km s^{-1} and $\dot{M}_A \sim 8.5 \times 10^{-4}$ $M_\odot$ yr^{-1} with the secondary (η Car-B) wind properties,

$V_{B\infty} \sim 3000$ km s^{-1} and $\dot{M}_B \sim 10^{-5}\, M_\odot$ yr^{-1} (Groh et al. 2012). Confirmation of the wind properties of η Car-B is important to establish proper relationships of the interacting winds and to demonstrate that three-dimensional (3D) hydrodynamical models describe the wind interactions correctly.

Direct detection of the companion star, η Car-B, has proven to be very difficult as η Car-A is estimated to be at least 100-fold brighter than η Car-B at visible and near-infrared wavelengths and the projected semimajor axis of the orbit is only 7 mas at the assumed distance of 2300 pc (Weigelt et al. 2007; Madura et al. 2012). 3D hydrodynamical simulations with radiative transfer applied to Hubble Space Telescope/Space Telescope Imaging Spectrograph (HST/STIS) spatially resolved spectra provided information about the binary orbit relative to the sky plane and the observer's line of sight (LOS) through analysis of the interacting wind structures (see Gull et al. 2009; Madura 2010; Madura et al. 2012, 2013 and references therein).

More recently, two studies determined that the brightening of η Car over the past half century is apparent, not intrinsic to the binary. Mehner et al. (2019) reviewed five decades of infrared photometry of the Homunculus and showed that the long-term change of its flux is minimal but with a possible modulation associated with the 5.54 yr binary period. Damineli et al. (2019) used ground-based visible photometry (with several millimagnitudes accuracy and easier to secure with higher cadence than from space) to show that the apparent brightening of η Car is due to material near the binary in the LOS that is dissipating and/or moving out of the LOS and predicted that this material will disappear by the mid-2030s. Over the past two decades, the equivalent width of Hα λ6563 has decreased by twofold (Mehner et al. 2015). Mehner et al. (2015) argued that the change was due to latitudinal changes in the mass-loss rate, while Damineli et al. (2021) suggest that it is related to the disappearance of the foreground occulter along the LOS.

Previous photometric studies in the UV have been limited to the mid- and near-UV. Martin & Koppelman (2004) and Martin et al. (2006) measured the increasing brightness of η Car using HST Advanced Camera for Surveys direct imagery through UV filters longward of 2000 Å combined with synthetic photometry derived from STIS CCD spectra extending from 1854 Å longward recorded from 1998–2004. Davidson et al. (2018) utilized STIS echelle spectra recorded between 2002 and 2016 to estimate the increased flux in the 1770–2200 Å spectral interval. Photometric measures of the flux below 1700 Å have been limited to spectroscopic studies by the International Ultraviolet Explorer (Viotti & Rossi 1999) and direct detection of the 900–1180 Å flux by the Far Ultraviolet Spectroscopic Explorer at two epochs (during ingress into the X-ray eclipse, and several months later). Iping et al. (2005) found that the flux shortward of Lyα disappeared during ingress, and suggested that the observed flux in this region at the later epoch arises from the companion star, η Car-B.

While the central source has increased in brightness, the fluxes from the Weigelt clumps, located within 0.3″ of η Car did not brighten (Gull et al. 2009; Mehner et al. 2010), also indicating that the obscuring material, likely an obscuring clump in the LOS, is relatively close to the binary (Weigelt et al. 1995). CMFGEN models of the primary star suggested that the obscuring material appeared to be covering the central portion of the primary star but less so the outer wind where most of the Hα λ6563 emission occurs (Hillier 2011; Damineli et al. 2021). Recent measures by Weigelt et al. (2021) indicate that the structures seen in H I Br α λ4.05 μm emission extend 23 mas beyond the wind structure seen in continuum, measured to be 6 mas in diameter.

Groh et al. (2010) found evidence for wind absorption as high as -1900 km s^{-1} in the metastable He I λ10830 absorption profile as η Car approached periastron in 2009 and demonstrated similar, but weaker absorptions in the STIS FUV echelle spectra that were recorded leading up to the periastron in 2003. The optical He I lines have also been observed to have high-velocity absorption components, but have not been observed to go to as high in velocity as the He I λ10830 (Richardson et al. 2016).

Because of the declining absorption (Damineli et al. 2019), we concluded that as the periastron event of 2020 approached, we would be able to see more deeply into the central binary especially in the FUV (1150–1700 Å). Thus, we organized an observing campaign in coordination with the Chandra X-ray Observatory using the HST/STIS[17] to monitor spectral variations across the periastron passage centered in February 2020.

These observations displayed significant changes in the FUV spectra recorded across the 2020 February periastron passage (herein defined as Periastron 14) that, in hindsight, were marginally detectable in the FUV spectra recorded across the 2003 July periastron passage (Periastron 11). Unfortunately, no data were obtained in the FUV during the two intervening periastron passages of 2009 February and 2014 August.

In this paper, we present FUV photometry derived from new and archived HST/STIS observations. The observations and reductions are described in Section 2. Resolution of the spectral fluxes into photometric intervals separated into bands of absorption and continuum islands is described in Section 3. A brief discussion is presented in Section 4 followed by conclusions in Section 5. Three spectra, selected from the late high-ionization state, just before periastron, and deep in the low-ionization state associated with periastron, from both Periastrons 11 and 14, are displayed in the Appendix with highlighted spectral intervals used for the photometric measures discussed in this paper.

2. The Observations

A series of eight HST visits were conducted in coordination with Chandra X-ray Observatory observations following X-ray spectroscopic changes across η Car's periastron event in 2020 February (D. Espinoza et al. 2022, in preparation). The visits were scheduled (1) to establish a baseline of spectral changes as the binary approached periastron and (2) to sample changes near periastron, following the drop in ionization state of the primary wind and multiple shells associated with the Homunculus (Gull et al. 2006). Across each periastron, the hot secondary star plunges deep into the primary wind. Its ionizing FUV radiation, plus FUV radiation from the wind–wind collision shock cone, is temporarily blocked. The dates of observations and relevant binary orbital phases are listed in Table 1.

[17] Based on observations made with the NASA/ESA HST, obtained (from the Data Archive) at the STSI, which is operated by the Association of Universities for Research in Astronomy, Inc., under NASA contract NAS5-26555. These observations are associated with programs 12013 and 12750 and previously archived programs.

Table 1
Log of HST/STIS Observations

Date	MJD	Phase, ϕ[a]	Aperture[b]
Periastron 11			
2002-01-20[c]	52294.2	10.736	$0.3'' \times 0.2''$
2002-07-04[c]	52459.8	10.818	$0.3'' \times 0.2''$
2003-02-13[c]	52683.3	10.928	$0.3'' \times 0.2''$
2003-05-26[c]	52785.8	10.979	$0.3'' \times 0.2''$
2003-06-01[c]	52791.1	10.982	$0.3'' \times 0.2''$
2003-06-22[c]	52812.4	10.992	$0.3'' \times 0.2''$
2003-07-05[c]	52825.1	10.998	$0.3'' \times 0.2''$
2003-07-29[c]	52849.7	11.010	$0.2'' \times 0.2''$
2003-09-21[c]	52903.4	11.037	$0.3'' \times 0.2''$
2004-03-06[c]	53070.3	11.119	$0.3'' \times 0.2''$
Periastron 14			
2018-04-21[c]	58229.1	13.670	$0.2'' \times 0.2''$
2019-05-14[d]	58617.9	13.862	$0.3'' \times 0.2''$
2019-07-02[d]	58666.8	13.886	$0.2'' \times 0.2''$
2019-08-25[d]	58720.6	13.913	$0.2'' \times 0.2''$
2019-10-15[d]	58771.6	13.938	$0.2'' \times 0.2''$
2019-12-28[d]	58845.9	13.975	$0.2'' \times 0.2''$
2020-02-08[d]	58887.3	13.995	$0.2'' \times 0.2''$
2020-03-09[d]	58917.4	14.010	$0.2'' \times 0.2''$
2020-03-11[c]	58919.4	14.011	$0.2'' \times 0.2''$
2020-04-01[d]	58940.3	14.022	$0.2'' \times 0.2''$
2021-01-26[c]	58940.6	14.170	$0.2'' \times 0.2''$

Notes.
[a] Phase, ϕ, refers to binary phase based upon both disappearance of He II emission and X-ray drop with periastron passage numbered 13 occurring on MJD (24)56874.4 and orbital period of 2022.7 days (Teodoro et al. 2016). Grant et al. (2020) using a Keplerian radial velocity model found that the actual periastron occurs 4 days earlier. The periastron number refers to the convention established in Damineli et al. (2008) based upon spectroscopically detected periastrons beginning in 1948 February.
[b] Spectra using the unsupported aperture $0.3'' \times 0.2''$ were extracted with STIS Instrument Definition Team software for a stellar source. Spatial extractions correspond to $0.0875''$ width excluding the nebular contributions.
[c] Archive spectra recorded with E140M (1150–1710 Å) and E230M (1610–2300 Å). Nominal resolution: $R = \lambda/\delta\lambda = 40{,}000$.
[d] Spectra recorded with E140H (1150–1680 Å) using settings 1234, 1416, and 1598 Å. Nominal resolution: $R = 109{,}000$.

A previous series of STIS FUV spectra were recorded as part of an extensive Hubble Treasury Program at similar binary phases across Periastron 11 (Table 1). Comparison of the archived and new FUV spectra shows that the FUV brightness of η Car has increased tenfold since 2002 as discussed in Section 3.4. Additional archived STIS FUV and mid-UV spectra, relevant to this discussion, are also included in Table 1.

While the medium-resolution echelle modes, E140M and E230M ($R = \lambda/\delta\lambda = 40{,}000$), had previously been appropriate to monitor the spectral changes from 1150–2350 Å, the increased FUV fluxes led to predicted global photon count rates for the Multi-Anode-Multi-Array (MAMA) detectors for the E140M and E230M echelle modes that potentially exceeded the MAMA safety limits. We therefore switched to using the higher dispersion echelle mode, E140H ($R = 109{,}000$), to decrease the detector global count rates, which limited observations in a single HST orbit visit to three cross-dispersed grating settings. We chose to monitor the most important resonance lines of C IV, Si IV, C II , and Si II within the 1150 and 1680 Å spectral range with three grating settings: 1234, 1416, and 1598 Å.

Two additional FUV spectra were independently recorded with the E140M grating across Periastron 14. As they are in the public domain, they were included in this study. One E140M spectrum was recorded within 2 days of the E140H spectrum ($\phi = 14.010$ and 14.011). The reduced spectra are quite similar, confirming our ability to intercompare spectra obtained in the two spectral modes.

The spectra recorded across Periastron 14 were reduced via standard pipeline processing provided by STScI for a point source in the one-dimensional format (X1D). However, η Car has substantial nebular and extended wind emission close to the star that can contribute to background if the background extraction region is not carefully chosen. The first visit at $\phi = 13.862$ utilized the $0.3'' \times 0.2''$ aperture, which led to some nebular contamination in the intra-order background for the cross-disperser grating set at 1234 Å. The net effect, much smaller than that noted for Periastron 11 observations as the star increased tenfold in brightness relative to the nebular structure, was that completely saturated absorption profiles had slightly negative fluxes that were corrected before comparisons were made. Otherwise, the spectrum recorded at $\phi = 13.862$ is quite similar to spectra recorded at other phases leading up to Periastron 11. Measured fluxes used in this study were consistent with minimal flux changes leading up to Periastron 14.

We confirmed that the FUV E140M and E140H modes have been carefully monitored using standard stars since the STIS installation in HST in 1997. Variations in flux with the standard $0.2'' \times 0.2''$ aperture, used for all but one observation across Periastron 14, are consistent with standard star monitoring that demonstrated instrument stability with measured flux variations below 4%, well below the variation of η Car flux measures across the two periastrons. All spectra recorded across Periastron 11 were reduced with the special stellar extraction tool, while all spectra recorded across Periastron 14 were reduced by standard pipeline processing. Thus the reduction techniques are internally consistent for each periastron.

Most observations recorded across the 2003 May (Periastron 11) event were accomplished with the $0.3'' \times 0.2''$ aperture (690 au × 460 au at 2300 pc distance) for which STScI did not provide supported reductions. The STScI X1D extractions led to overcorrection of background due to extended wind, projected to be close to the stellar core, which led to negative fluxes of about 10% for saturated resonance lines especially at the shorter wavelengths where the echelle orders are closer together on the detector format. Instead, a spatially defined, line-by-line extraction was used to obtain the stellar component with the STIS Instrument Development Team software tools. In order to exclude the nebular components on both sides of the extended aperture, an extraction strip with a $0.0875''$ width centered on the stellar component was used for all spectral extractions across Periastron 11. Agreement of special extractions to the standard X1D spectral extractions for spectra recorded across Periastron 11 with the $0.2'' \times 0.2''$ aperture proved to be excellent. This application was subsequently carried over to the STScI data analysis and is publicly available as documented by Valenti et al. (2002). This tool provides a better solution for estimating background, leading to residuals for the saturated resonance lines that are less than 1% of the nearby flux, well below the photometric variations described below.

3. FUV Photometric Measures across the Two Periastrons

3.1. Overview

The most striking difference in spectra recorded from before Periastron 11 through Periastron 14 is the roughly tenfold increase in flux. Despite this increase in flux level, the spectra, especially during the high-ionization state, are quite alike. In particular, they indicate a similar ionization, and show similar wind emission profiles. As discussed by Damineli et al. (2021), the changes in flux are likely due to the dissipation of an occulter along our LOS. However, it is unclear whether the change in the occulter is attributable to changes in one, or both, stars, or is simply due to the long-term evolution of the occulter. The long-term flux changes are discussed further in Section 3.4.

However, a closer examination of the spectra does show significant changes. In particular, we note by Periastron 14 the disappearance of numerous narrow-width absorption lines originating from four velocity systems in the −100 to −300 km s^{-1} velocity range detected in the STIS NUV by Gull et al. (2006) and the nearly complete disappearance of the ≈800 strong absorption lines of H_2 at −513 km s^{-1} identified by Nielsen et al. (2005) in the high-ionization states before and after Periastron 11. This disappearance is consistent with the dissipation of the occulter—more UV from the secondary star is reaching the absorption systems within the Homunculus, increasing the ionization in the low-velocity systems and destroying the H_2 in the Homunculus shell.

Of more interest are changes in spectra across periastron. Photometry derived from FUV spectra recorded by HST/STIS across Periastron 11 (Figure 1, left column) showed a large drop across Periastron 11 and slow recovery toward the pre-periastron levels 9 months later. While the drop was consistent across the entire FUV, the flux in most spectral intervals dropped significantly more (factor of 5, Figure 1, top left) than in others (factor of 2, Figure 1, bottom left). This behavior can be contrasted with that seen across Periastron 14. First, the flux prior to periastron was less variable. Second, as for Periastron 11, many bands showed a significant drop (factor of three) across periastron (Figure 1, Top right). However, some bands showed an increase, followed by a sharp drop, in flux, similar to that seen in the *V* band (Figure 1, bottom right).

To understand the variable fluxes and their implications we rigorously define, in Section 3.2, spectral intervals, labeled as absorption bands and continuum islands, that illustrate the different flux variations between periastrons, and across a given periastron. We also give a broad overview of their properties, highlighting the spectra in two contrasting bands (Section 3.3). The absorption bands are dominated by strong transitions. We highlight the overall properties in Section 3.3.1. Changes in the velocity profile of a resonant Si II line are discussed in Section 3.3.2 and comparisons are made of the velocity profiles for three Si II doublets in Section 3.3.3. Bands that show similar behavior to the *V* band are discussed in Section 3.3.4. Plots of representative spectra are presented in Figures A1–A6 and their wavelength intervals are listed in Table A1.

3.2. Defining the Absorption Bands and the Continuum Islands

Closer examination of the spectra recorded across Periastron 14 (bottom plots in Figures A1–A6) revealed unanticipated variations. Specifically the spectrum recorded on 2020 February 8 ($\phi = 13.995$) showed flux increases in relatively narrow wavelength intervals (4–18 Å in width) primarily between 1400 and 1540 Å relative to that recorded at $\phi = 13.975$, while most flux measures below 1400 Å and above 1600 Å decreased . The flux dropped in a relatively uniform way across the spectrum recorded at $\phi = 14.010$ with substantial recovery noticeable by $\phi = 14.022$. In contrast, the fluxes in spectra recorded at similar phases across Periastron 11 decreased more and exhibited a slower recovery than that observed across Periastron 14.

We examined three spectra at $\phi = 13.975$, 13.995, and 14.010 as shown in Figures A1–A6. We separated specific wavelength intervals by changes in flux between $\phi = 13.975$ and 13.995.

1. Wavelength intervals, where the flux dropped at $\phi = 13.995$ relative to the flux measured at $\phi = 13.975$. Because these intervals have signatures of strong absorptions from the extended wind and intervening shells of the Homunculus we call these *absorption bands*. As demonstrated in Sections 3.3.1–3.3.3, these absorption bands are spectral windows with strong signatures of absorptions originating from the extended winds and the intervening Homunculus shells.
2. Wavelength intervals, where the flux increased at $\phi = 13.995$ relative to flux measured at $\phi = 13.975$. We call these *continuum islands*. Note that these continuum islands are spectral intervals where strong, singly ionized resonant and near-resonant absorptions are absent. However, weak emission and absorptions are still located within in these spectral intervals. The continuum islands are basically portions of the FUV spectrum less affected by absorptions of cooler, intervening gas.
3. Both absorption band and continuum island fluxes dropped in the spectrum recorded at $\phi = 14.010$ relative to the fluxes recorded at $\phi = 13.975$.

Using these three spectra, we identified absorption bands and continuum islands throughout the 1150–1680 Å spectral region as listed in Table A1. Two spectral intervals, an absorption band and a continuum island, are presented in Figure 2 and are discussed in the next section.

The integrated fluxes for these selected spectral intervals were measured and normalized setting the observational fluxes at $\phi = 10.979$ and 13.913 to unity. These normalized fluxes are plotted in Figure 1 along with a similarly normalized flux for the *V*-band (5500 Å) measurements of the central core (Damineli et al. 2021). Plots of the photometry for individual spectral intervals are displayed in Figure A7.

The absorption bands, displayed in the top two plots in Figure 1, dropped to similar levels (60%–70% below pre-periastron levels) with slow recovery across both periastrons. Recovery in flux levels after Periastron 14 began sooner than after Periastron 11.

The continuum islands, displayed in the bottom two plots in Figure 1, behaved quite differently. Across Periastron 11, the continuum island fluxes declined slightly from $\phi =$ 10.928–10.992, marginally increased by 10% at $\phi = 10.998$ and dropped 40% by $\phi = 11.010$. Recovery in flux was slow even at $\phi = 11.034$ and reached the pre-periastron level before $\phi = 11.119$, 9 months after periastron. The entire drop in flux for the continuum islands across Periastron 11 was significantly less than for the absorption bands.

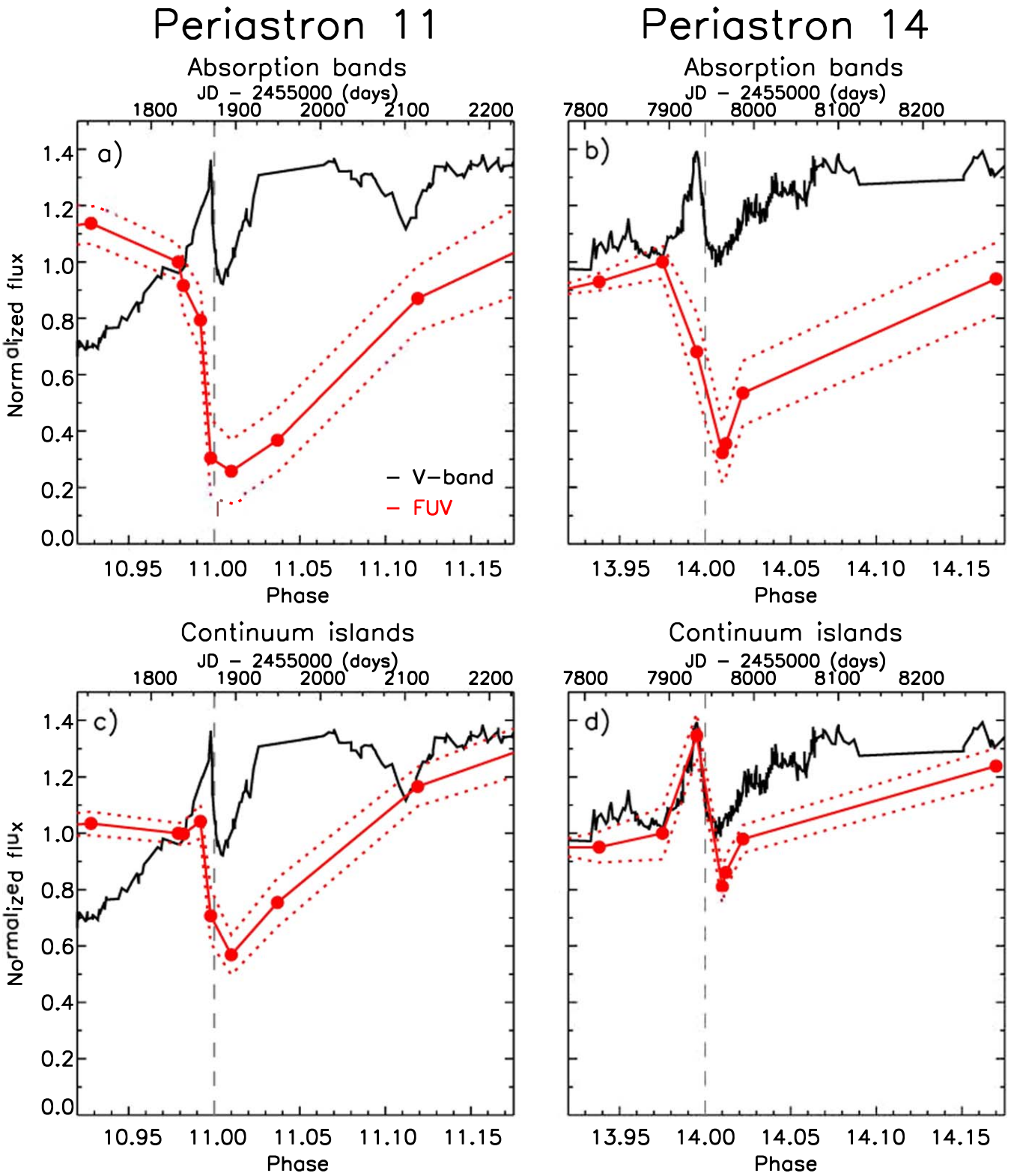

Figure 1. Comparison between the FUV (red curve) and the optical *V*-band (black curve) light curves across Periastrons 11 (left) and 14 (right) for the absorption bands (top) and continuum islands (bottom, see definition in the text). The photometry curves were normalized near phase $\phi = 0.98$ in all panels. The data points for the FUV correspond to the average flux of selected absorption bands and continuum islands from 1240–1680 Å, with 1σ error estimates, are connected by the red filled and dotted–dashed lines, respectively. The vertical gray dashed line refers to the orbital phase, $\phi = 0.000$, at which time the He I disappears and the X-ray flux falls dramatically (Teodoro et al. 2016).

Across Periastron 14, the continuum island flux levels increased by 40% between $\phi = 13.975$ and 13.995, dropped by 40% of the peak level, with near recovery by $\phi = 14.022$. By $\phi = 14.170$, the flux had exceeded the pre-periastron flux by 20%. The continuum island variations are in synchrony with flux variations measured in the *V* band across Periastron 14.

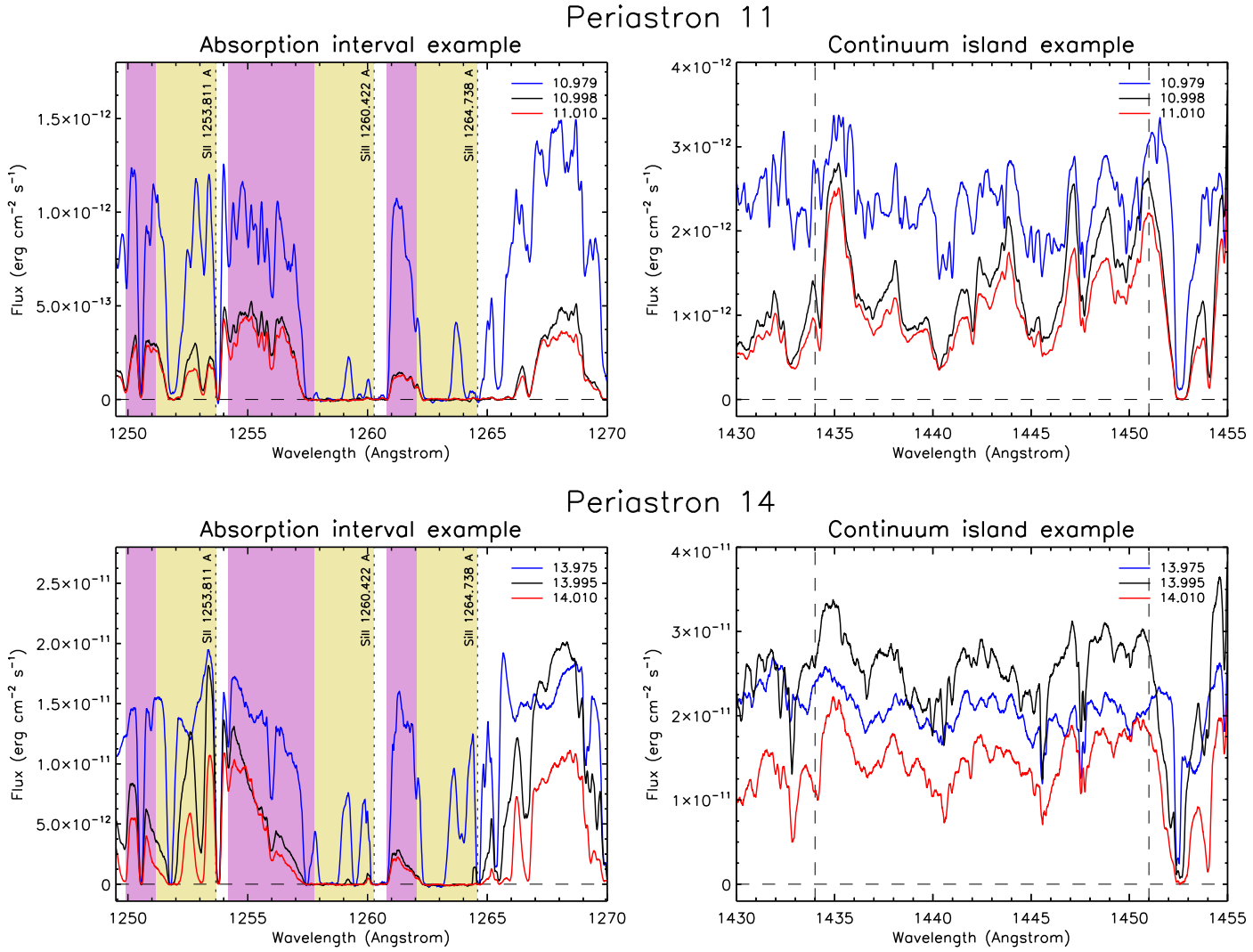

Figure 2. Examples of an absorption band and a continuum island for Periastron 11 (top row) and Periastron 14 (bottom row). Segments of three spectra are plotted with the convention of late high-ionization state (blue: $\phi = 10.979$, 13.975), just before periastron (black: $\phi = 10.998$, 13.995) and deep in the low-ionization state (red: $\phi = 11.010$, 14.010). The left column displays the spectral region including part of the λ1260.2 absorption band (1243–1277.5 Å). Two Si II lines and one S II line with associated blueshifted absorption complexes are present in this absorption band. The light yellow backgrounds highlight the 0 to -600 km s^{-1} absorption bands for each of the Si II and S II lines. The light purple backgrounds highlight the -600 to -900 km s^{-1} absorptions for the S II λ1254 and the Si II 1265 lines and the -600 to -1475 km s^{-1} absorption for the Si IIλ1260 line. The right column displays the spectral region including the λ1442.5 continuum island (1434–1451 Å delimited by vertical dashed lines). No strong lines have yet been identified but modulation of the continuum strongly suggests absorption lines possibly originating from deeper layers of η Car-A. All photometric intervals are displayed in Figures A1–A6 and listed in Table A1.

3.3. Characterizing of the FUV Absorption Bands and Continuum Islands

Examination of the spectra recorded across Periastrons 11 and 14 revealed multiple complexes of absorption from 1150–1320 Å and from 1600–1670 Å. A closer look at these absorption bands (Figures A1–A6) revealed strong changes in resonant and near-resonant absorption lines across velocities ranging from 0 to -1500 km s^{-1}, which include contributions from the primary (η Car-A) wind absorptions, 0 to -420 km s^{-1}, as determined by Groh et al. (2012), and narrow absorptions from intervening shells within the Homunculus (Gull et al. 2006). Absorption at higher blueshifted velocities up to -1500 km s^{-1} appeared across Periastron 14.

Figure 2 provides examples of one absorption band and one continuum island for both periastrons. Each panel displays a spectrum before periastron ($\phi = 10.979$ and 13.975), which is characteristic of the late phase of the high-ionization state, a spectrum just before periastron ($\phi = 10.998$ and 13.995) and a spectrum just past periastron when the flux drops deeply ($\phi = 11.010$ and 14.010).

3.3.1. Example of an Absorption Band

An absorption band, labeled 1260.2 Å in Table A1 and shown in Figure A2, extends from 1243–1277.5 Å. We show a portion of this absorption band across the two periastrons in Figure 2, left column. The most prominent absorption lines are two Si II lines, a resonant line, 1260.422 Å, and a near-resonant line, 1264.738 Å, originating from an energy level 287 cm^{-1} above the ground state, and one S II line, a resonant line at 1253.811 Å, which is noticeably weaker.

Across Periastron 11, the general effect, as seen in the absorption of the two Si II lines relative to the spectrum at $\phi = 10.979$, is an overall drop in continuum plus near complete absorption from 0 to -600 km s^{-1} by $\phi = 10.998$. This strong

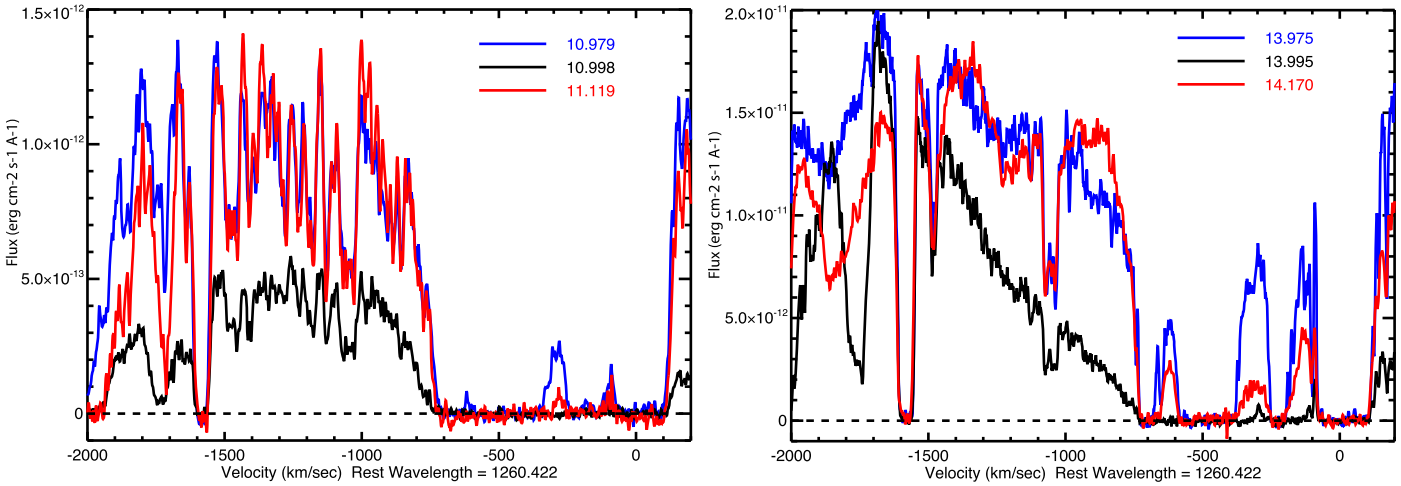

Figure 3. Velocity plots of the Si II λ1260 resonant line absorptions compared for Periastrons 11 and 14. Left: comparison of a high-ionization pre-periastron state (blue: $\phi = 10.79$), a near periastron (black: $\phi = 10.998$), and a post-periastron high-ionization state (red: $\phi = 11.119$). The pre- and post-periastron absorptions are nearly identical. The near periastron flux appears to drop uniformly compared to the high-ionization state profiles. Two weak spikes of continuum (-100 and -300 km s^{-1}) seen at $\phi = 10.975$ disappear near periastron and reappear weakly post-periastron. Right: comparison of a high-ionization pre-periastron state (blue: $\phi = 13.975$), a near periastron state (black: 13.995), and a high-ionization post-periastron state (red: $\phi = 14.170$). The absorption wing declines linearly from -700 km s^{-1} to nearly -1500 km s^{-1} in contrast to Periastron 11. Three continuum spikes are readily apparent at -100 to -200 km s^{-1}, -250 to -400 km s^{-1}, and -500 to -575 km s^{-1}. The flux levels of these three continuum spikes have not fully recovered by $\phi = 14.170$, but the high-velocity wind has disappeared. The three plots are in absolute flux units.

absorption continued through $\phi = 11.010$ and is identifiable in multiple resonant and near-resonant lines at various strengths.

The increase in ionizing UV flux between Periastrons 11 and 14 led to significant spectral changes across both the high-ionization and low-ionization states. This led to the disappearance of numerous narrow absorption lines originating from four velocity systems in the -100 to -300 km s^{-1} velocity range detected in the STIS NUV by Gull et al. (2006), and the nearly complete disappearance of the ≈800 strong absorption lines of H_2 at -513 km s^{-1} identified by Nielsen et al. (2005).

The changes across Periastron 14 were significantly different compared to the variations seen during Periastron 11. Across Periastron 14, few absorptions from singly ionized ions in the -100 to -300 km s^{-1} systems could be identified in the FUV spectra. A very limited number of weak H_2 absorptions lines are present in the FUV spectra recorded by STIS across Periastron 14.

By $\phi = 13.995$, strong absorption had set in. The absorption across 0 to -600 km s^{-1} is nearly total for the Si II lines, but not complete for the weaker S II line. However the absorption is not uniform, but extends from full absorption by -600 km s^{-1} decreasing by -900 km s^{-1} where other absorption lines cut off additional information. All three strong absorbing lines show this characteristic. However, for the Si II 1260.422 Å the decreasing absorption extends well beyond the -900 km s^{-1} to at least -1450 km s^{-1} before being cut off by the S II 1253.811 Å absorption.

This decline in absorption from saturation at -600 km s^{-1} decreasing toward blueshifted velocities is prevalent for the many singly ionized resonant and near-resonant absorptions across Periastron 14. In Section 3.3.2, we describe the absorption changes in one Si II resonant line across the two periastrons. In Section 3.3.3, we compare the behavior of three Si II doublets in the recorded spectra in an effort to gain further understanding of this high-velocity absorption feature.

3.3.2. Changes in a Si II Velocity Profile between Periastrons 11 and 14

Figure 3 displays the changes of one relatively isolated resonant line, Si II λ1260, across the two periastrons.

In general, the FUV spectrum drops near periastron across Periastron 11 and returns to pre-periastron levels as demonstrated in Figures 1 and A1–A5. Changes across the velocity range of the Si II λ1260 reflect this as can be seen by the relatively flat drop in flux levels at velocities more negative than -700 km s^{-1} (Figure 3, Left). Weak continuum spikes (-100 and -300 km s^{-1}) are present in the high-ionization state as notable at $\phi = 10.975$ and weakly at $\phi = 11.119$.

By Periastron 14, the apparent FUV flux in our LOS has increased tenfold, which affected the intervening absorbers. The Si II λ1260 resonant absorption changes considerably (as displayed in Figure 3, right). The wing of the blueward absorption line profile changes from total absorption at -700 km s^{-1} decreasing in absorption linearly up to -1500 km s^{-1}. The apparent continuum spikes are much stronger both before and after periastron ($\phi = 13.975$ and 14.170), but nearly zero in amplitude near periastron ($\phi = 13.995$). Such is consistent with the absorbers between -100 and -375 km s^{-1} being at least doubly ionized in the high-ionization state but recombining during the low-ionization state brought on by the primary wind absorbing the ionizing UV across periastron.

3.3.3. Behavior of Three Si II Doublets across Periastron 14

The P Cygni absorption wing decreases blueward from -600 km s^{-1} as seen in for multiple resonant and near-resonant lines of singly ionized elements but is often blended with the many superimposed absorption lines in the FUV.

One clear set of examples arises from three Si II doublets, rising from the ground state and from an energy level 287 cm^{-1} above the ground state, that are located in the STIS FUV spectral range (1150–1680 Å). The resonant line-velocity

profiles are plotted in Figure 4, left column, along with the paired, near-resonant line-velocity profiles as plotted in Figure 4, right column.

The 0 to -600 km s^{-1} velocity intervals are expected to show a smooth P Cygni profile dominated by the primary wind with terminal velocity of -420 km s^{-1} as modeled by Groh et al. (2012). However, narrow velocity absorptions within the Homunculus from singly ionized metals arise from over 30 discrete velocities inventoried by Gull et al. (2006) from 0 to -600 km s^{-1} in NUV spectra leading up to and across Periastron 11. Excitation temperatures, derived from the lower levels of the absorbing transitions, ranged from 720–5000 K with the lower temperatures associated with the most blue-shifted shells. Resonant and near-resonant absorptions of these same ions in the STIS FUV are much stronger and across Periastron 11 blended as displayed in Figure 3, left.

However, the FUV flux, as measured by STIS, increased nearly tenfold during the high-ionization state preceding Periastron 14, leading to increased ionization of the lower velocity shells, located closest to η Car. Most metals became doubly ionized leading to much less absorption, especially from 0 to -250 km s^{-1}. The outer shells, moving at -385 km s^{-1} and higher speeds, remained singly ionized, leading to continued strong absorptions. As a result, spikes of continuum are seen across the 0 to -380 km s^{-1} velocity range at $\phi = 13.97$ in Figure 3, but by $\phi = 13.995$, with the drop of FUV flux, the absorptions increased to near saturation from 0 to -600 km s^{-1}, and again decreased by $\phi = 14.170$.

The most noticeable change in the velocity profiles is at blueshifted velocities exceeding -600 km s^{-1} (Figure 4). At $\phi = 13.975$ all six Si II absorption profiles show significant flux at these velocities, but by $\phi = 13.995$ absorption is saturated through -600 km s^{-1} decreasing with increasing blueshifted velocity. The near-resonant lines, arising from 287 cm^{-1} are cut off at -900 to -1200 km s^{-1} by the companion resonant absorption, but the resonant absorption profiles extend to at least -1300 km s^{-1}. For the Si II λ1260 and the Si II λ1264.7 lines, the absorption wind extends to -1500 km s^{-1} in a strikingly linear behavior. Although the absorption profiles of the other two double pairs follow each other well, they are blended with other lines originating from intervening shells within the Homunculus.

After making allowance for the influence of other lines, it is apparent from Figure 4 that the shape and strength of the high-velocity absorption is similar for all lines. Since the oscillator strengths, *gf*, values differ by over an order of magnitude between the doublets (e.g., $gf = 2.43$ for the λ1260 transition compared to $gf = 0.266$ for the λ1527 transition, Table 2) this indicates that while the absorption structures are optically thick (otherwise the line depth would correlate with *gf*), individually they do not cover the FUV source completely. The most likely cause of this absorption is material related to the colliding winds. The sudden appearance, then subsequent disappearance of the absorption across periastron is caused by the orbital motion of the binary system leading (1) to the cutoff of the FUV radiation as the secondary star dives deeply into the primary wind and (2) to the reemergence of the secondary star post-periastron as η Car-B emerges from the primary wind on the far side of η Car-A. Despite the large variance of *gf* values between transitions in each doublet (see Table 2), the general slope is maintained.

Throughout the high-ionization state, our LOS from the binary is within the ionized cavity carved out by the secondary wind (Madura et al. 2012, 2013) with the trailing edge of the bowshock then crossing our LOS as periastron approaches. The wind interaction region includes a nearly continuous absorption velocity distribution ranging from the -420 km s^{-1} primary wind to the ≈ -3000 km s^{-1} secondary wind. However, as periastron approaches, the FUV radiation from the hot secondary star is cut off leading to recombination of the interacting wind regions. Either a series of clumps or a near-continuous ribbon of gas, relaxing in ionization passes through our LOS, as revealed in the low-ionization absorptions of Si II doublets.

3.3.4. Continuum Island Variations

The continuum island, labeled 1442.5 in Table A1 and displayed in Figure A4, is plotted in more detail in Figure 2, right column. At $\phi = 13.995$, this spectral interval increased in flux relative to previous phases as exemplified by the spectrum at $\phi = 13.975$ and post phases as exemplified by the spectrum at $\phi = 14.010$. Within several continuum islands, complex structures change both in amplitude and velocity across Periastron 14. Specific line identifications have thus far been unsuccessful. We focused instead on the changes in continuous fluxes.

Across Periastron 11 (Figure 2, upper right), the continuum island flux between 1430 and 1455 Å decreased from $\phi = 10.975$–10.998 and stayed at the same level at $\phi = 11.010$, consistent with the photometry plotted in Figure 1.

Across Periastron 14 (Figure 2, lower right), the continuum island flux increased at $\phi = 13.995$ compared to those recorded at $\phi = 13.975$, then decreased by 14.010, while fluxes in the absorption bands decreased at $\phi = 13.995$ and remained weak at $\phi = 14.022$.

The potential sources of additional FUV flux are the hot inner wind of the primary, the companion star and the colliding wind shock. At phase 13.995, the enhancement in the FUV can either be coming from the companion or from the inner wind of the primary. 3D hydrodynamical modeling of the interacting winds demonstrates that the companion star is within its wind-blown cavity across the entire high-ionization state and directly in our LOS until just before periastron when it plunges deeply within the primary wind (Gull et al. 2011; Madura et al. 2012, 2013). Likewise, the interacting wind structures are visible in our LOS until the primary begins to block our view near periastron. The sudden appearance of the FUV enhancement at 13.995, when the secondary is deep within the primary wind, indicates that the source of the FUV is most likely the inner wind of the primary star. However the wind–wind collision zones might contribute some continuum flux. Groh et al. (2010) noted high-velocity absorptions in lines of C IV $\lambda\lambda$1548, 1550 and Si IV $\lambda\lambda$1394, 1403 leading up to Periastron 11, which originate in the wind–wind shocks.

3.4. Long-term Changes in FUV Flux between High-ionization and Low-ionization States

Several sets of STIS UV spectra, observed across two decades at similar orbital phases were located in the HST archives. Two pairs of spectra are displayed in Figure 5 along with their flux ratios. One pair was recorded in the high-ionization state ($\phi = 10.73$ and 13.67, Figure 5, top left) and

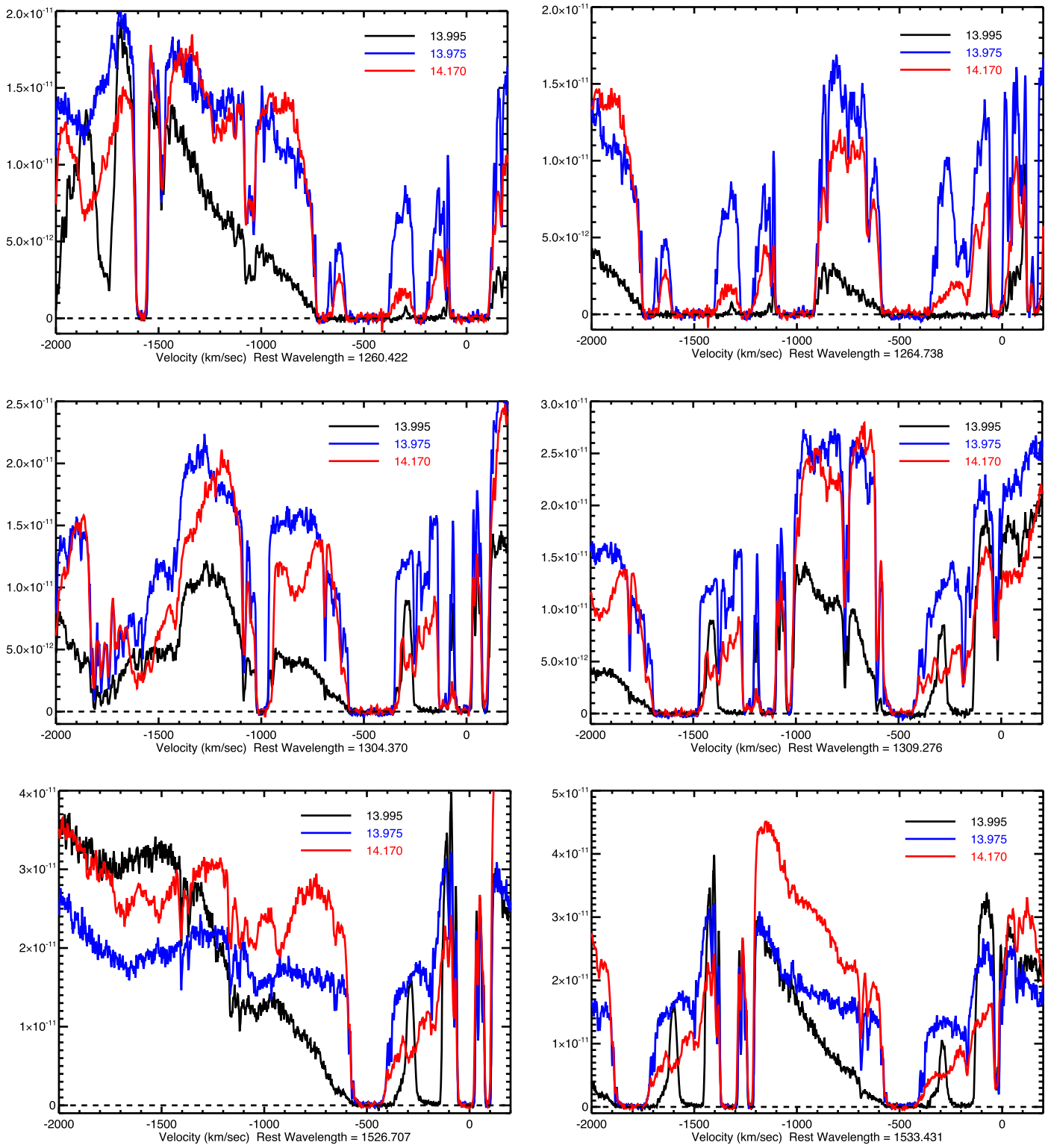

Figure 4. Velocity plots of three Si II doublets listed in Table 2. Plotted are a late, high-ionization state spectrum (blue: $\phi = 13.975$), a near periastron spectrum (black: $\phi = 13.995$), and an early recovery high-ionization state spectrum (red: $\phi = 14.170$). While absorption in portions of the 0 to -600 km s^{-1} velocity range are saturated, the absorption profiles for the three phases across Periastron 14 are strikingly similar at velocities blueward of -600 km s^{-1} despite large differences in *gf* values. This indicates that the absorbing material is optically thick, but in the form of clumps that do not fully cover the FUV source in our LOS. The velocity distribution extending from -600 to nearly -1500 km s^{-1}, demonstrates that the absorbers are within the high-velocity, interacting wind structures which pass through our LOS across periastron. Each resonant profile plotted in the left column is paired with its near-resonant profiles, arising from 287 cm^{-1} above the ground state, plotted in the right column. Note that the doublets are very close in wavelength with separations only 4–7 Å (1000–1700 km s^{-1}), so the near-resonant profiles are cut off above -900 to -1200 km s^{-1} by the resonant line profiles.

Table 2
Si II Doublet Transition Data

λ[a] (Å)	gf[b]	E_l (cm^{-1})	E_u (cm^{-1})	Terms
1260.422	2.43	0	79,338	$^2P^o_{1/2}$ –$^2D_{3/2}$
1264.738	4.36	287	79,356	$^2P^o_{3/2}$ –$^2D_{5/2}$
1265.002	0.452	287	79,338	$^2P^o_{3/2}$ –$^2D_{3/2}$
1304.370	0.186	0	76,665	$^2P^o_{1/2}$ –$^2S_{1/2}$
1309.276	0.320	287	76,665	$^2P^o_{3/2}$ –$^2S_{1/2}$
1526.707	0.266	0	65,500	$^2P^o_{1/2}$ –$^2S_{1/2}$
1533.431	0.532	287	65,500	$^2P^o_{3/2}$ –$^2S_{1/2}$

Notes.
[a] All data abridged from NIST version 5.8, 2020 October 30 at https://physics.nist.gov/asd.
[b] The intrinsic absorption strength of a transition is proportional to the gf value, where f is the oscillator strength and g the statistical weight of the lower level. Note the gf values for the 1260.422 and the 1264.738 Å transitions demonstrate that the transition from the ground (0 cm^{-1}) is half as strong as that for the transition originating from 287 cm^{-1} above the ground state.

another pair was recorded in the low-ionization state ($\phi = 11.012$ and 14.012, Figure 5, top right). All spectra, originally recorded at high dispersion ($R = \lambda/\delta\lambda = 40{,}000$), were smoothed to a 5 Å resolution to evaluate gross spectral variations.

During the high-ionization state, the flux ratio is relatively flat from 1400-2350 Å despite the eight-fold increase in flux that occurred from 2003–2019 (Figure 5, lower left). Shortward of 1400 Å, the flux ratio increases with a drop/spike across the saturated, circumstellar H I Lyα absorption. With dissipation of the occulter in LOS, less metals are in singly ionized state leading to less absorption at the shorter wavelengths. Note the excess emission for $\phi = 13.67$, on the blue-side of the highly saturated H I Lyα absorption, which suggests decreased column density in the LOS, consistent with the dissipating occulter.

During the low-ionization state, the flux ratio steepens considerably toward shorter wavelengths. The individual spectra, recorded at nearly identical orbital phase, 11.012 and 14.012, each drop to shorter wavelength (Figure 5, top right) and the flux ratio (Figure 5, bottom right) systematically increases to shorter wavelengths reaching nearly 100-fold below H I Lyα, well above that seen in the high-ionization ratio.

The increased slope during the low-ionization state, compared to the high-ionization state (Figure 5) occurs when the high-velocity wings of the resonant and near-resonant absorptions from neutral and singly ionized atoms increase. These atomic species rapidly recombine when the FUV flux from η Car-B is cut off by the extended wind of η Car-A.

4. Discussion

Isolation of the FUV spectrum into absorption bands and continuum islands is a new concept that promises to provide considerable insight on the apparent changes of the FUV flux of η Car over the past two decades. In simplest terms, the absorption bands are regions where strong resonant and near-resonant absorptions from singly ionized atoms are located. The continuum islands are where there are fewer, weaker absorptions. However, portions of some continuum islands are modulated by broad absorptions that appear to shift with orbital phase in a manner much like the velocity shifts seen in the higher Balmer lines studied by Grant et al. (2020). The continuum islands are consistent with flux originating from deeper within the primary stellar wind and possibly with contributions from both the wind–wind interaction region and the secondary star. Additional studies especially across future periastrons should lead to improved insight on these processes.

Figure 6 provides two sketches describing the sources of absorption in LOS from η Car near apastron (top) and near periastron (bottom). As the binary orbit of η Car has a high eccentricity ($e = 0.9$), the hot, less massive η Car-B spends most of the orbit near the apastron distance from η Car-A (≈30 au). 3D modeling of the interacting winds (Madura 2010), combined with HST/STIS spatially resolved emission-line spectra, determined that periastron occurs with η Car-B located on the far side of η Car-A (Gull et al. 2011).

For most of the orbital period, η Car-B is located on the nearside of η Car-A carving out a highly ionized cavity at an orientation such that our LOS to the primary passes through the cavity (Figure 6, top). The ionizing UV radiation escapes this cavity and illuminates the Homunculus. As the FUV and ionizing UV increased between Periastrons 11 and 14, an increasing number of low-velocity systems, closest to η Car, changed from singly ionized to more highly ionized state across the high-ionization state of η Car.

For a few months η Car-B approaches η Car-A plunging deeply into the primary's extended wind, which absorbs the bulk of the ionizing UV radiation. At periastron, η Car-B is within 1–2 au of η Car-A located on the far side of the primary (Figure 6, bottom).

The multiple velocity systems within the Homunculus, as sketched in Figure 6 were affected by ionizing UV across Periastron 11. Two velocity systems are associated with the Great Eruption in the 1840s (−513 km s^{-1}) and the Lesser Eruption in the 1890s (−146 km s^{-1}). The −513 km s^{-1} system was seen in multiple lines of many singly ionized ions with a kinetic temperature of 760 K along with ≈800 H_2 absorption lines in the FUV. Most of the H_2 absorption lines disappeared across Periastron 11 due to the drop of FUV radiation, but reappeared post-Periastron 11.

The −146 km s^{-1} system was seen in multiple lines of many singly ionized ions with a kinetic temperature of that changed from 6400 K during the high-ionization state to 5000 K during the low-ionization state and back to 6400 K across Periastron 11. Across Periastron 11, absorptions from Ti II appeared, then disappeared indicating that ionizing radiation >13.6 eV had temporarily disappeared within the Little Homunculus across Periastron 11 (Gull et al. 2006).

Very different changes in ionization and excitation occurred across Periastron 14. Most of the H_2 absorption lines were no longer present across the high-ionization state, indicating that most of the H_2 has been destroyed in the 16.6 yr between Periastron 11 and 14. Likewise most of the narrow line absorptions from singly ionized metals in the −146 km s^{-1} system were absent during the high-ionization state. Across Periastron 14, some weak absorptions did briefly reappear at −146 km s^{-1} (K. Nielsen et al. 2021, in preparation).

Evidence that the increase in ionizing radiation affected the multiple shells within the Homunculus is also present in the resonant and near-resonant lines like the Si II as shown in Figure 3. The continuum spikes in the −100 to −400 km s^{-1}

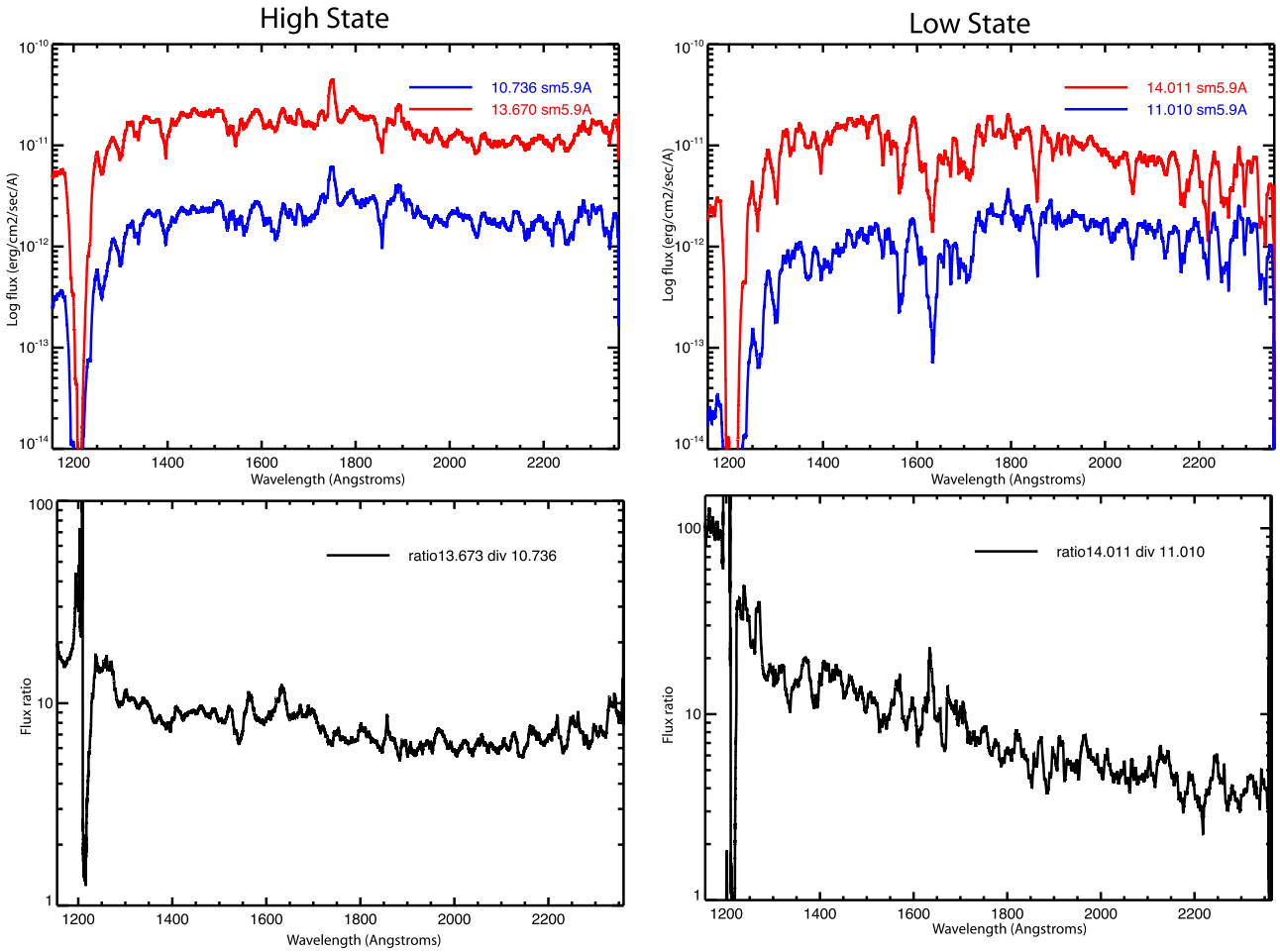

Figure 5. Comparisons of fluxes and flux ratios past apastron (high-ionization state) and after periastron passage (low-ionization state). These two pairs of HST/STIS spectra were recorded 16.6 yr apart at similar orbital phases. The spectra have been smoothed to 5.9 Å resolution (top) and the subsequent ratio is displayed (bottom). The increase in slope, shown in the bottom right plot, is due to decreased absorptions of resonant and near-resonant lines in singly ionized and neutral gas by Periastron 14 relative to Periastron 11. Despite the huge change in the flux levels, the same spectral features are present across both cycles 11 and 14. The deep absorption feature centered at λ1216 in the flux plots is due to H I Lyα.

velocity range are consistent with the low-velocity shells becoming at least doubly ionized across the high-ionization state. The near disappearance of these continuum spikes across Periastron 14 indicates that these shells briefly drop to a singly ionized state, then become more highly ionized during the recovery to the high-ionization state.

The high-velocity (-400 to -600 km s^{-1}) absorptions in the resonant and near-resonant lines remain saturated indicating that the ionizing UV radiation has not reached the outer shells of the Homunculus, again consistent with what is observed in the narrow line absorption systems (K. Nielsen et al. 2021, in preparation).

4.1. Previous Evidence of Resonant Absorptions

The photometric measurements demonstrate that the mechanism which causes the flux drop in the absorption bands is distinct from that causing the spike/dip in the continuum islands. Both occur when η Car-B plunges deeply into the very extended wind of η Car-A.

The resonant line absorptions, as demonstrated in Figure 2, increase in strength for velocities ranging from 0 to at least -1500 km s^{-1}, at least a factor of 3 higher than the terminal velocity of the wind of η Car-A ($V_{\rm Ainf} \approx 420$ km s^{-1}, Groh et al. 2012). Similar high-velocity absorption leading up to Periastron 12 in 2009.1, up to -1800 km s^{-1} in He Iλ10830 had been noted by Groh et al. (2010) and across Periastron 13 in 2014.6 in the lines of He I $\lambda\lambda$4716, 5876, 7065 up to -800 km s^{-1} (Richardson et al. 2016). Groh et al. (2010) also noted increased absorptions in Si IV $\lambda\lambda$1394, 1403 up to -2100 km s^{-1} leading up to Periastron 11 and in Si II $\lambda\lambda$1527,1522 and C IV$\lambda\lambda$1548, 1550, C II $\lambda\lambda$1334, 1335 only up to -1200 km s^{-1}. This is the first time similar high-velocity absorption across a periastron event has been reported in the FUV.

4.2. Changes in FUV Flux in the Long Term

Comparison of the flux ratios for high- and low-ionization states in Figure 5 is consistent with the increased absorptions by neutral and singly ionized atoms during the low-ionization state. This indicates that the column density of singly ionized atoms decreased since Periastron 11, while the FUV flux has increased tenfold.

The increase and decrease of the continuum islands for Periastron 14 follow in concert with the spike and drop of the *B*-band flux which was well described by Madura & Owocki (2010) and Madura & Groh (2012) to be caused by a *borehole*, the cavity created by the wind of η Car-B in the inner wind of

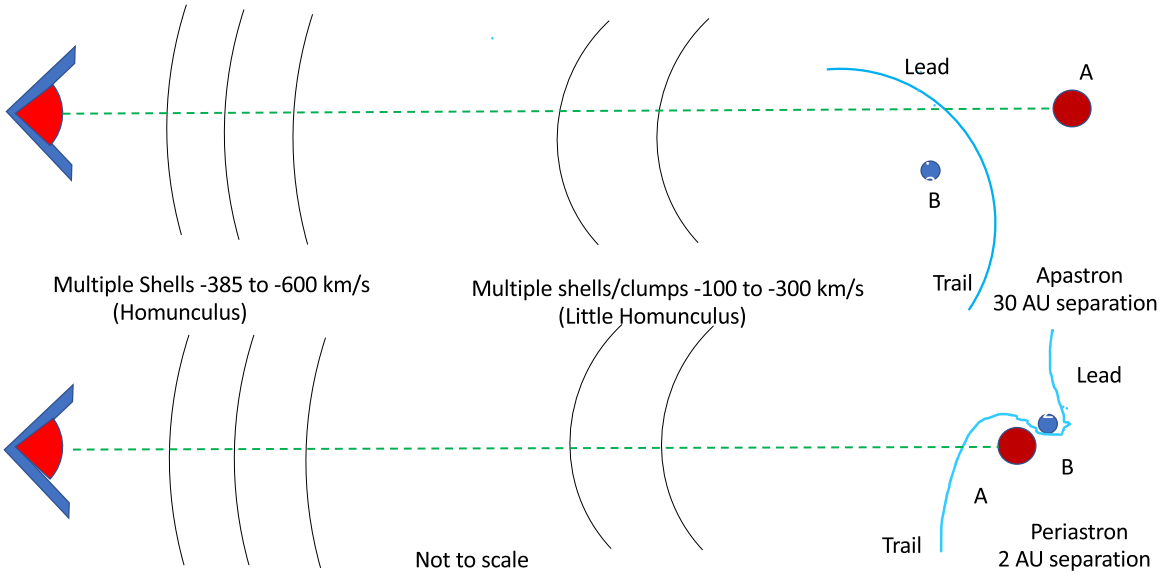

Figure 6. Two diagrams depicting structures in LOS from η Car. Top: geometry of system near apastron. Our LOS is through the cavity blown by the wind of η Car-B and ionized by its FUV radiation. The leading arm (Lead) and the trailing arm (Trail) defines the boundary between the two colliding winds and are the primary source of X-radiation. Bottom: geometry of the system near periastron. η Car-B has plunged deeply into the extended primary wind of η Car-A leading to complete cutoff of the ionizing UV shortward of 912 Å and at periastron is within 1–2 au of η Car-A. The trailing arm is ill-defined as the terminal velocity of η Car-B (3000 km s^{-1}) far exceeds the terminal velocity of η Car-A (420 km s^{-1}) creating a spatially dispersed-with-velocity collision zone. The gas in the trailing arm relaxes to singly ionized states with resonance and near-resonant absorptions dropping with negative velocity simply due to $1/R^2$ dispersal. The apparent increase of FUV radiation, brought on by the vanishing occulter, ionizes multiple shells/clumps in LOS between -100 and -300 km s^{-1} to higher ionization states as shown by the narrow emission seen within the Si II resonant/near-resonant absorptions in that velocity range. During the low-ionization state, across periastron, the ionizing UV flux is cut off, leading to strong absorptions in the -100 to -300 km s^{-1} velocity range.

η Car-A. As η Car-B penetrates into the primary wind, the cavity enables radiation from the deeper, hotter layers of η Car-A's inner wind to escape in our LOS. Emissions/absorptions from the interacting wind structures and η Car-B itself may also contribute to the FUV spectrum.

The 3D hydrodynamic models of Madura et al. (2012, 2013) also show that our LOS is through the hot, ionized cavity carved by η Car-B near apastron. As the stars approach periastron passage, the trailing arm of the wind interaction zone passes through our LOS, then for weeks, the undisturbed primary wind enters our LOS and finally the leading arm of the wind–wind shock cone cuts off the primary wind for the next high-ionization state supported by the hot, secondary star, η Car-B. The primary wind at apastron has a terminal velocity of 420 km s^{-1} (Groh et al. 2012) so we might expect a P Cygni-shaped profile with that limiting velocity, but the wind absorption is complicated by the absorption shells within the Homunculus that modulate between -122 and -600 km s^{-1} (Gull et al. 2006). Additionally, the primary wind terminal velocity may be decreased by the secondary wind and its photospheric UV emission.

Absorptions at velocities blueward of -600 km s^{-1} must be produced by the secondary stellar wind throughout the high-ionization state (≈ -3000 km s^{-1}, Pittard & Corcoran 2002), and especially near periastron, by the trailing arm of the shock cone. This arm is expected to begin crossing our LOS around $\phi = 0.92$. It is ionized by the FUV radiation of η Car-B until it plunges deeply into the primary wind along its journey to periastron, which occurs when η Car-B has moved to the far side of η Car-A (Madura et al. 2013). Little evidence of the trailing arm is seen in the singly ionized absorptions until the drop in the FUV that occurs much closer to periastron. Based upon the *V*-band photometry, sampled with better time coverage than that of the STIS spectra, the drop begins just before $\phi = 0.98$.

The appearance of the trailing arm has been previously seen in absorptions of He I λ10830 leading up to Periastron 12 (Groh et al. 2010) and now confirmed by absorptions in FUV resonance lines leading up to Periastron 14. Richardson et al. (2016) followed the trailing arm in absorptions of visible-wavelength He I extending to -800 km s^{-1} leading up to Periastron 13. The He I absorptions track the location of the recombining helium in the presence of EUV radiation. With the loss of UV radiation at $E > 13.6$ eV, the trailing arm recombines to singly ionized states. The drop in flux of the FUV continuum islands also shows that the trailing arm relaxed in ionization.

Our LOS is about 45° out of the binary orbital plane. Across the high-ionization state the LOS crosses the secondary-wind cavity close to the highly curved, trailing arm. We expect that a small drop in $\dot{M}_A$, of the order of 10%–20%, would lead to a larger wind cavity carved by the wind of η Car-B with lower column density in our LOS leading to a drop in absorption. Detailed 3D models are necessary to confirm this suggestion. Alternatively, a fluctuation in the wind–wind interface due to clumping or other phenomena could cause a significant, stochastic change. Differentiating between long-term decrease in absorption and changes in the trailing arm or wind–wind variations require observations in the FUV across future periastron passages, especially after the foreground occulter has disappeared.

The flux ratios, measured in the high- and low-ionization states, indicate less neutral and singly ionized atoms were present across cycle 14 compared to cycle 11. This suggests that $\dot{M}_A$ has dropped between 2003 and 2020, increasing the size of the wind-blown cavity and briefly providing a deeper

view into η Car-A and the ionizing radiation from its inner, hotter atmosphere.

Across Periastron 14, a strong absorption appeared at blueshifted velocities exceeding -600 km s^{-1} that was much stronger than the absorption observed by Groh et al. (2010) at velocities up to -2100 km s^{-1}. Groh et al. (2010) attributed these high-velocity absorptions to the wind–wind interaction regions. The new FUV STIS spectrophotometry provided evidence that these high-velocity absorption components contribute to major drops in the FUV across periastron passage.

What changes have led to the very different photometric behavior in the FUV in the absorption bands and continuum islands?

1. A foreground occulter is dissipating and/or is nonuniform in obscuration. The photometric studies by Damineli et al. (2019) clearly show that the apparent flux of η Car is increasing with time, while the infrared studies by Mehner et al. (2019) demonstrate that the long-term bolometric luminosity has remained constant over the past five decades. The obscuring material, demonstrated by Damineli et al. (2019, 2021) to lie close to η Car, is clearly decreasing in optical depth but is this material an extension of the primary wind in our LOS? While small variations occur in the brightening trend, the long-term brightening has continued to increase. It may be that the occulter is an ejected clump of material in our LOS analogous to the three Weigelt clumps. We note that current observations and the [Fe II] and [Fe III] mappings of Gull et al. (2016) show that Weigelt B had apparently dissipated by 2014.
2. Apsidal motion in the highly elliptical orbit could cause a shift in the time of conjunction. The X-ray flux curve, followed over the past four orbital cycles has consistently reached minimum at the same orbital phase (Corcoran et al. 2017; Espinoza Galeas et al. 2021) to within a fraction of a day (Teodoro et al. 2016). Hirai et al. (2021) suggested that η Car was a three body system prior to the Great Eruption, an if so, we estimate a maximum residual apsidal motion of 3° per 5.54 yr orbit.
3. The change may be due to a decrease of η Car-A's mass-loss rate. The near constant bolometric luminosity (Mehner et al. 2019) implies a relatively constant primary mass-loss rate, but we caution that small changes in $\dot{M}_A$ of the order of 10%–20% over the past three cycles (16.6 yr) could mean a significant change in the wind structures in our LOS. A change in shape of the wind–wind collision shock should affect the X-ray spectrum, but the X-ray spectrum has not shown large variations through most of the orbit. The recovery from X-ray minimum has varied in strength and the phase minimum has varied in duration, which might have been caused by a change in emission measure near periastron passage of the hot, shocked gas due to either a change in mass-loss rate or stochastic change associated with the collapse and recovery of the colliding wind shock (Corcoran et al. 2010).
4. Although the dissipating occulter is the most likely cause, a change in mass-loss rate or apsidal motion (or some combination thereof) cannot be ruled out. Continued studies will be necessary to narrow down what is changing in the extended structures surrounding η Car in our LOS.

As we close this discussion, we point out that the FUV spectroscopic observations were recorded across only two periastron passages three cycles apart. No FUV observations were recorded across the two intervening periastrons. However changes in flux throughout the visible and near-red began during cycle 10 and continued through across the periastron passage 14. Damineli et al. (2019, 2021) demonstrate a long-term trend of increasing flux, which is predicted to continue until the early 2030s at which time the apparent coronagraph is expected to dissipate. We have sampled only two periastron passages well separated in time either of which could be anomalous in behavior. Only sampling in the FUV across future periastrons can confirm or not any long-term changes in FUV photometry.

5. Conclusions

UV spectroscopic observations of η Car across periastron passages 11 and 14 (in 2003 July and 2020 February) reveal a tenfold increase in the FUV flux, and more importantly, systematic flux variations across periastron. These observations suggest the following:

1. The minima in the absorption bands near periastron passage are the direct result of resonant absorptions from singly ionized elements in the outer regions of the binary system and its ejecta moving at velocities ranging from -100 to -300 km s^{-1}, as FUV radiation from η Car-B is temporarily engulfed by the inner wind of η Car-A across each periastron passage.
2. The atomic column density of the singly ionized absorptions has decreased between Periastrons 11 and 14 leading to deeper visibility in our LOS to the central region. Most likely this is caused by a decrease in total column density, but could in part be caused by higher ionization of the occulting material.
3. By Periastron 14, the visibility into the deeper layers of η Car-A led to detection of the borehole effect in continuum islands most prominently between 1400 and 1600 Å. The visibility of the borehole in *V*-band photometry changed by a smaller extent compared to previous periastrons (Damineli et al. 2021) suggesting a decline in FUV absorption with little change in visible band extinction.
4. These observations have provided a unique opportunity to probe into the deeper layers in the wind of a luminous blue variable (LBV) and the possibility of detecting information in the FUV of the interacting winds of the LBV and its companion.
5. Future FUV observations offer the potential of probing even more deeply the inner layers of η Car-A, the wind–wind interface, and possibly provide a direct detection of η Car-B.
6. Additional models of the hydrodynamics with radiative transfer are needed to improve our understanding of the wind interactions and the observations recorded here.

Future studies become all the more important as the central core of η Car is becoming more visible throughout the binary orbit. The additional FUV flux modifies the ionization of the previously ejected shells. Hopefully HST/STIS access will continue through the next decade allowing monitoring of changes across the next periastron (2025 July), which offers the potential of seeing even more deeply into the binary and interacting winds.

We thank the referee for much effort and useful comments that improved the presentation especially for those less familiar with η Car. We acknowledge funding from HST programs 15611 and 15992, which were accepted as supplementary observations associated with Chandra X-ray Observatory programs 20200564 and 21200197. M.F.C. is supported under the CRESST-II cooperative agreement #80GSFC17M0002 with the NASA/Goddard Space Flight Center. A.D. received funding from FAPESP 2019/02029-2. F.N. acknowledges FAPESP for support through process 2017/18191-8. A.J.F.M. is grateful for financial aid from NSERC (Canada).

Facility: HST(STIS).

Appendix
Selection of Absorption and Emission Photometry Intervals

Comparisons of spectra recorded immediately before the periastron ($\phi = 13.975$), close to the periastron event, ($\phi = 13.995$), and immediately after periastron, ($\phi = 14.010$), as expected, revealed two different responses across periastron:

1. Large spectral segments where the flux dropped. Most, if not all, of the flux drops can be attributed to increased absorption by singly ionized elements including Fe^+, C^+, S^+, and Ni^+. The bulk of these absorptions are below 1400 Å and between 1550 and 1670 Å.
2. Spectral segments where the flux increased at $\phi = 13.995$ (black) increased relative to the flux at $\phi = 13.975$. These changes are produced when the wind-blown cavity enters the deep inner layers of the extended primary wind, providing a glimpse of the wind–wind interactions across periastron. We named the regions of flux increases as continuum islands as they appear to be intervals containing weak absorptions isolated by intervals of strong absorptions. Most of the continuum islands are located between 1425 and 1520 Å.

Examples of selected absorption intervals (light yellow background) and continuum islands (light purple background) are presented in Figures A1–A6. Information on the selected absorption and continuum islands is listed in Table A1.

Figure A7 supplements Figure 1 by showing the wavelength behavior for each of the absorption bands and continuum islands identified in the spectra.

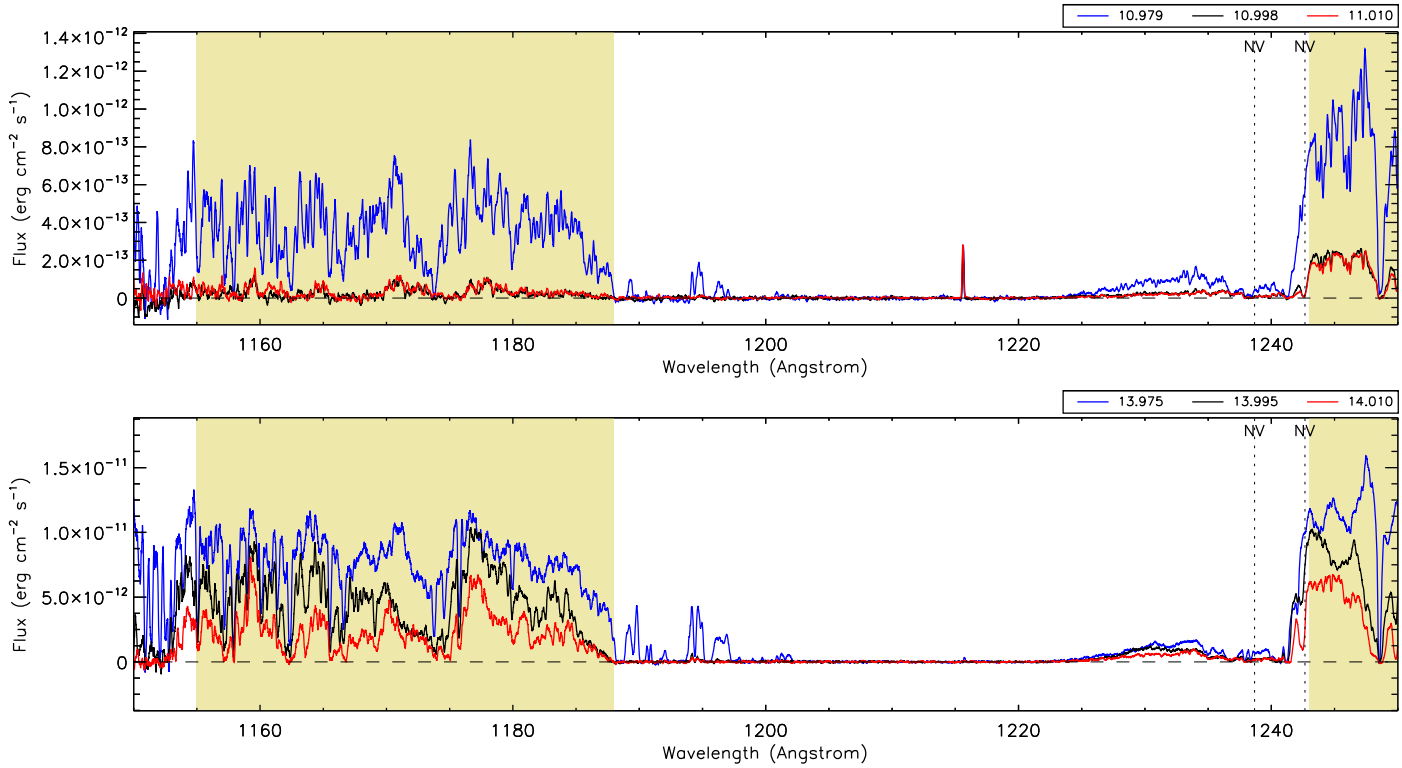

Figure A1. Selected absorption bands 1150−1250 Å. As reference for increase in apparent stellar flux, the geocoronal Lyα is quite weak in the measured fluxes across Periastron 14. The light yellow backgrounds highlight absorption bands. The tracing colors and corresponding numbers refer to the orbital phase. There is no continuum island in this spectral interval. Note the greater than tenfold difference in flux scales between the spectra plotted across Periastron 11 (top) and Periastron 14 (bottom). The spike at 1216 Å is geocoronal Lyα visible across periastron passage 11, but with the increase in FUV flux, minimal relative to η Car by periastron passage 14.

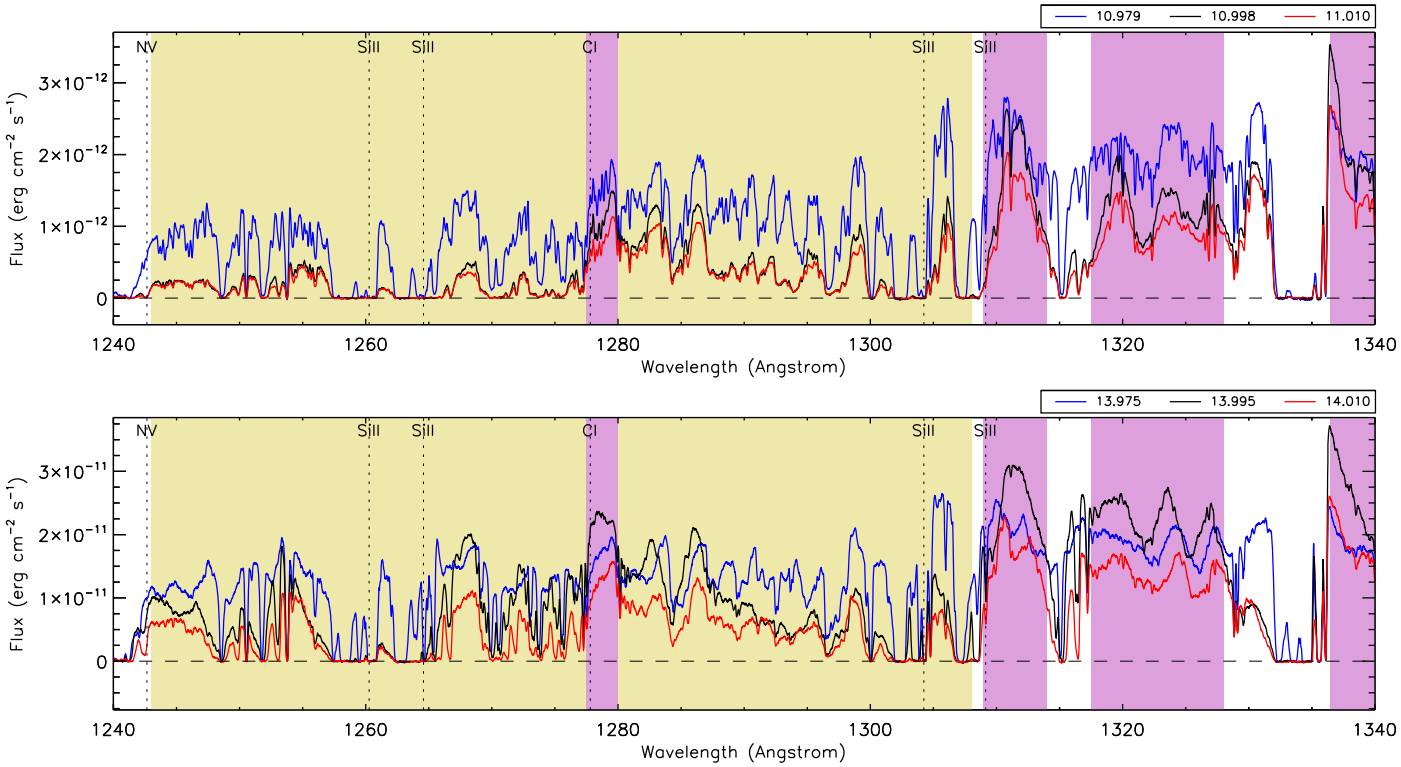

Figure A2. Selected absorption bands and continuum islands 1240−1340 Å. The light yellow backgrounds highlight absorption bands and the light purple backgrounds highlight the continuum islands. The tracing colors and corresponding numbers refer to the orbital phase. Note the tenfold difference in flux scales between the spectra plotted across Periastron 11 (top) and Periastron 14 (bottom).

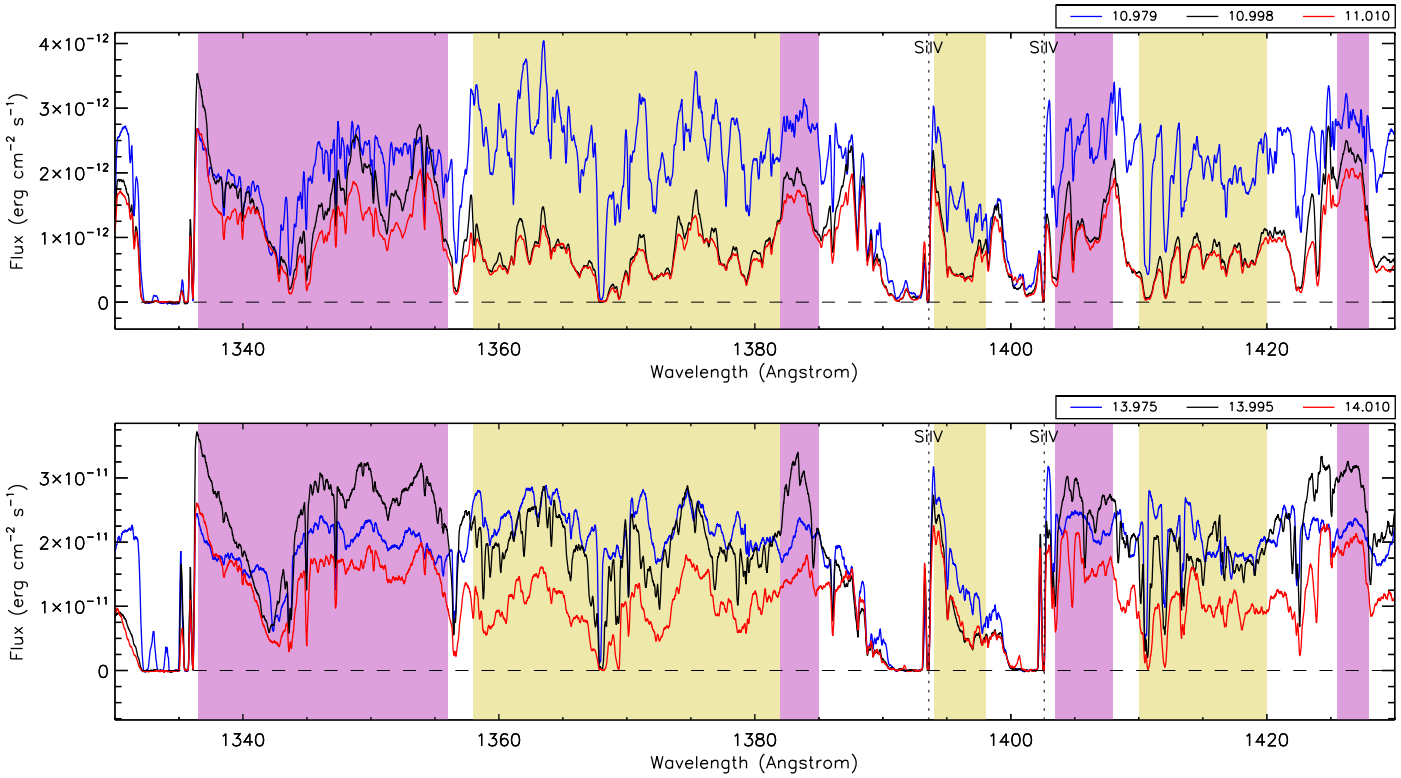

Figure A3. Selected absorption bands and continuum islands 1330−1430 Å. The light yellow backgrounds highlight absorption bands and the light purple backgrounds highlight the continuum islands. The tracing colors and corresponding numbers refer to the orbital phase. Note the tenfold difference in flux scales between the spectra plotted across Periastron 11 (top) and Periastron 14 (bottom).

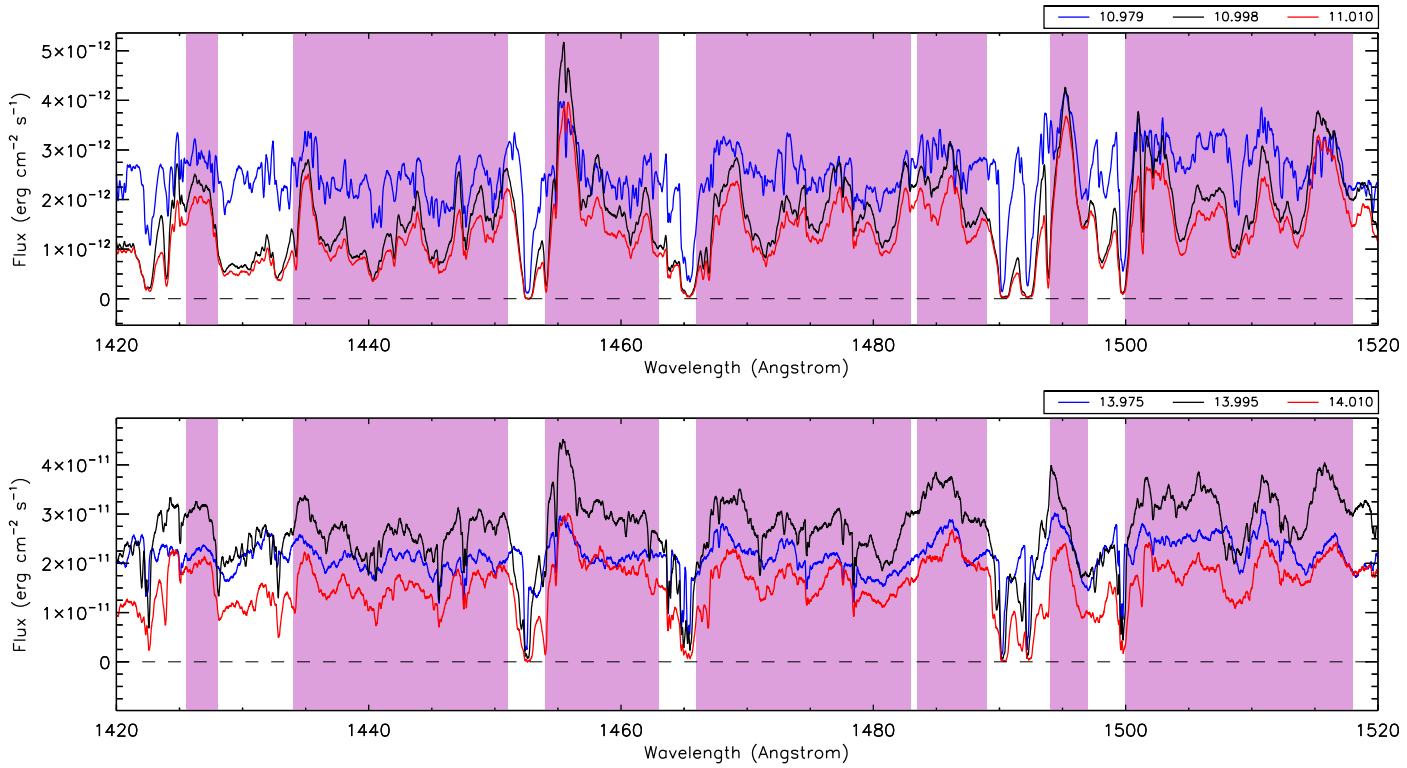

Figure A4. Selected absorption bands and continuum islands 1420−1520 Å. The light purple backgrounds highlight the continuum islands. The tracing colors and corresponding numbers refer to the orbital phase. Note the tenfold difference in flux scales between the spectra plotted across Periastron 11 (top) and Periastron 14 (bottom).

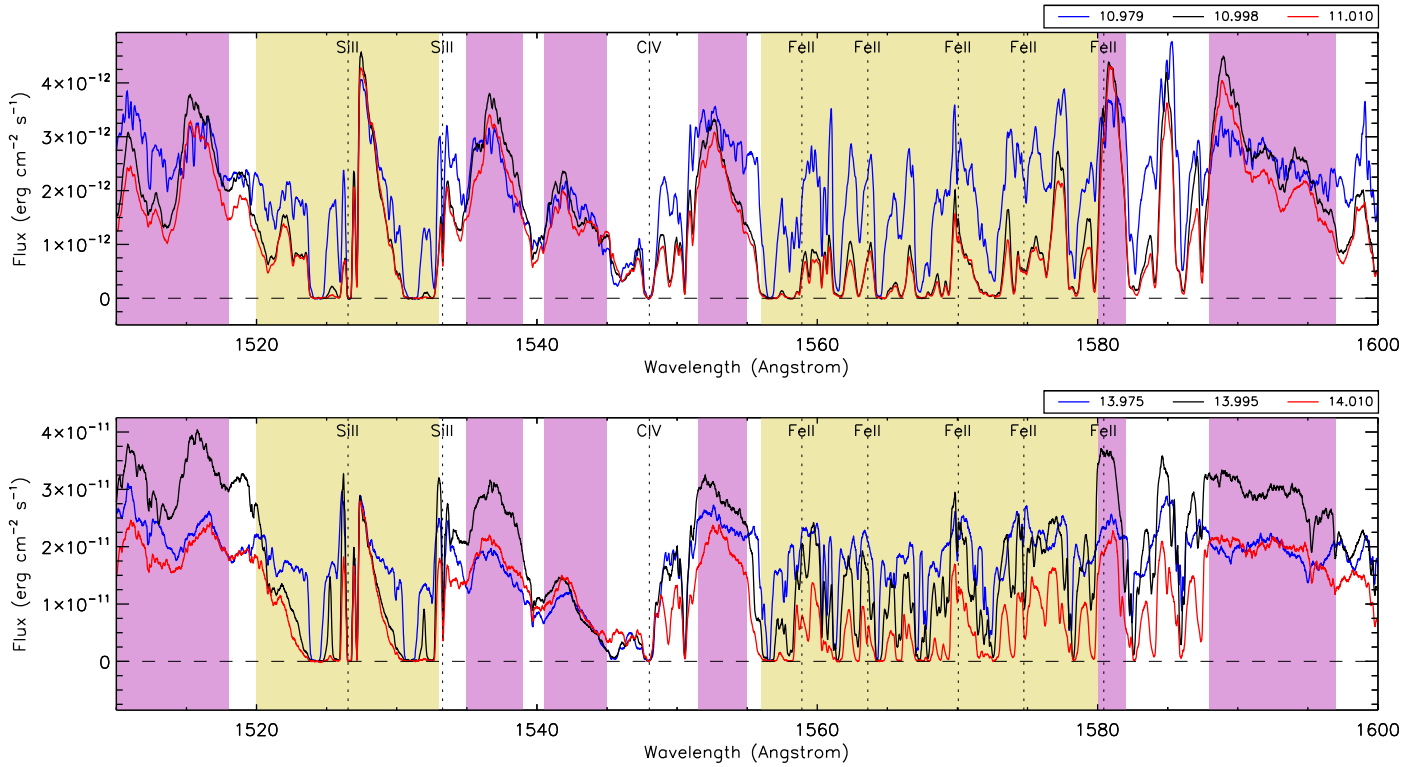

Figure A5. absorption bands and continuum islands 1466−1548 Å. The light yellow backgrounds highlight absorption bands and the light purple backgrounds highlight the continuum islands. The tracing colors and corresponding numbers refer to the orbital phase. Note the tenfold difference in flux scales between the spectra plotted across Periastron 11 (top) and Periastron 14 (bottom).

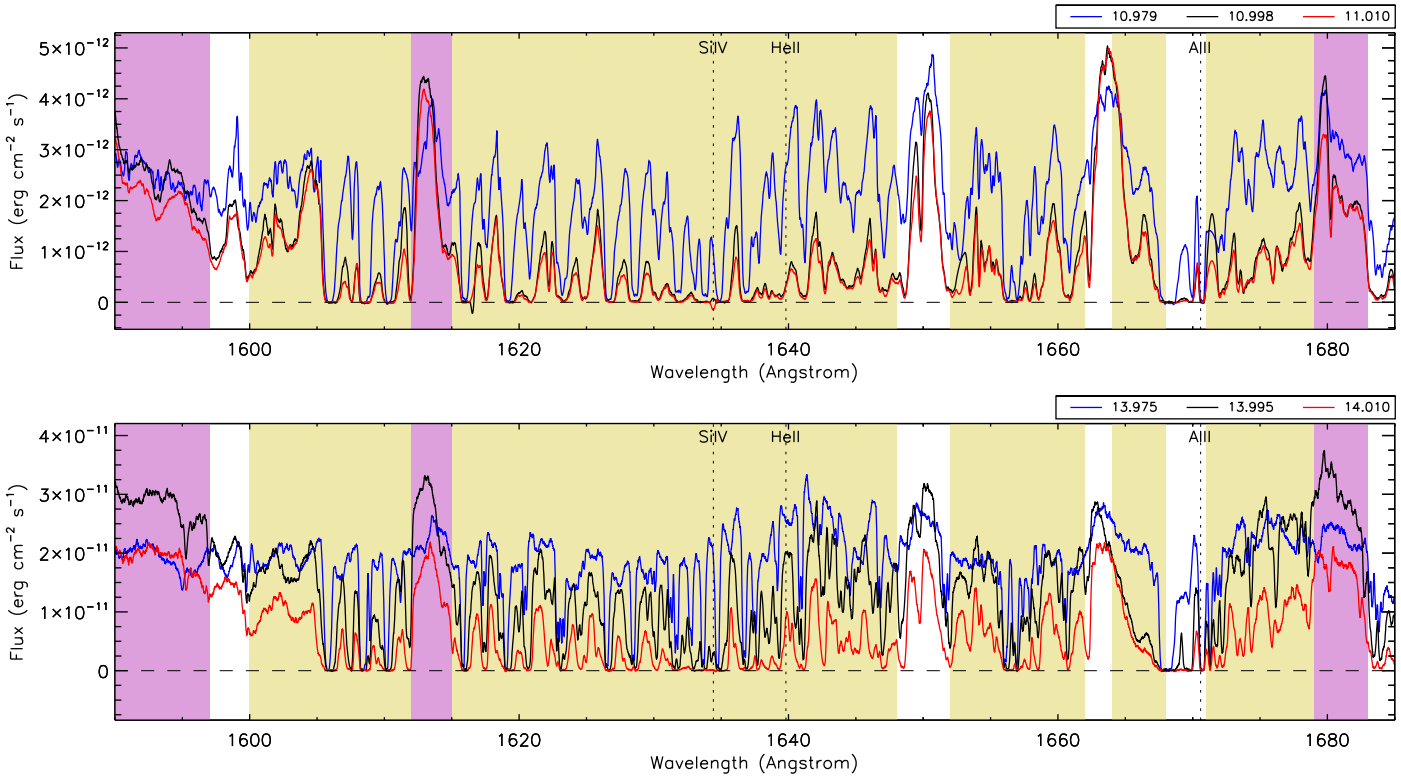

Figure A6. Absorption and emission intervals 1548−1685 Å. The light yellow backgrounds highlight absorption bands and the light purple backgrounds highlight the continuum islands. The tracing colors and corresponding numbers refer to the orbital phase. Note the tenfold difference in flux scales between the spectra plotted across Periastron 11 (top) and Periastron 14 (bottom).

Table A1
Absorption Bands and Continuum Islands

Central Wavelength (Å)[a]	Integration Interval (Å)	Comment
Absorption intervals (yellowish regions)		
1171.5*	1155–1188	Far UV resonances below Lyα
1260.2*	1243–1277.5	Includes Si II $\lambda\lambda$1265, 1260 and S II λ1254
1294*	1280–1308	Multiple resonance absorptions
1370	1358–1382	Includes Si II $\lambda\lambda$1304, 1309
1396+	1394–1398	Si IV blueshifted absorptions
1415*	1410–1420	Multiple resonance absorptions
1526.5+	1520–1533	Includes Si II $\lambda\lambda$1526, 1533
1568*	1556–1580	Multiple Fe II resonance absorptions
1606*	1600–1612	Multiple resonance absorptions
1631.5*	1615–1648	Multiple absorption resonances covering He II λ1640 Å
1657	1652–1662	Multiple resonance absorptions
1666+	1664–1668	Includes Al II λ1670 Å blueshifted absorption
1675*	1671–1679	Includes red side of Al II
Continuum islands (purple regions)		
1278.7*	1277.5–1280	Narrow continuum peak.
1311.5	1309–1314	Narrow continuum peak.
1322.7	1317.5–1328	Multiple peaks that shift in velocity across periastron
1346.3	1336.5–1356	Red side of C II resonance, velocity shifting feature
1383.5*	1382–1385	Peak Fe III and Al III transitions
1405.7	1403.5–1408	Continuum
1426.8*	1425.5–1428	Broad continuum
1442.5*	1434–1451	Continuum
1458.5*	1454–1463	Peak at Ni II red feature, continuum
1474.5	1466–1483	Many resonance absorptions of C I in this region
1486.2	1483.5–1489	C I-free continuum region
1495.5	1494–1497	Continuum
1509*	1500–1518	Complex features with velocity shifts
1537 +	1535–1539	P Cygni red component of nonresonant line
1542.8+	1540.5–1545	P Cygni red component of nonresonant line
1553.2	1551.5–1555	Red component of C IV λ1549 Å
1581	1580–1582	Continuum
1592.5*	1588–1597	Continuum
1613.5	1612–1615	Continuum
1681	1679–1683	Continuum

Note.
[a] * denotes absorption and emission intervals plotted in Figure A7. + denotes intervals including blueshifted components of resonance lines plus nonresonant P Cygni profiles.

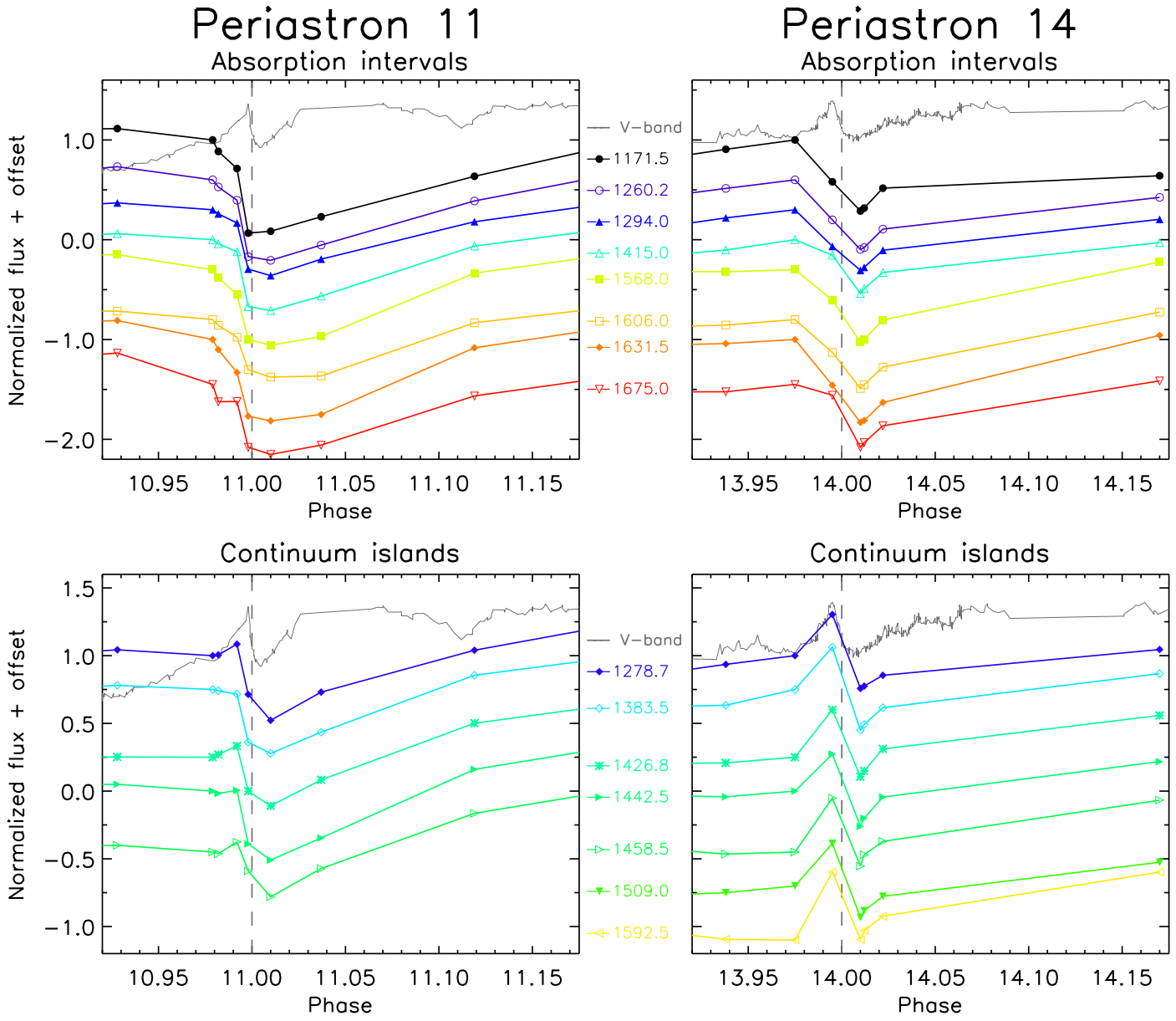

Figure A7. FUV photometry extracted from STIS FUV spectra recorded across Periastrons 11 (left) and 14 (right). The *absorption bands* measure changes in regions densely populated with low-ionization resonance transitions (upper row of plots). The continuum islands are spectral regions where flux increases at $\phi = 13.995$ relative to fluxes at $\phi = 13.975$ (lower row of plots). They include continuum and higher-excitation lines originating deeper within the η Car-A wind, the interacting wind region and possibly η Car-B. Across Periastron 11 (left column) absorption and continuum islands decline, bottoming out at $\phi = 11.010$, then returning to pre-periastron levels. A small peak is evident in the continuum islands at 10.993. Across Periastron 14 (right column), the absorption bands decline similar to that across Periastron 11, but the continuum islands (bottom right) show a spiked increase at $\phi = 13.995$ with a short dip at $\phi = 14.010$, which tracks the borehole peak/dip as seen in the *V*-band photometry, scaled for comparison.

ORCID iDs

Theodore R. Gull https://orcid.org/0000-0002-6851-5380
Felipe Navarete https://orcid.org/0000-0002-0284-0578
Michael F. Corcoran https://orcid.org/0000-0002-7762-3172
Augusto Damineli https://orcid.org/0000-0002-7978-2994
Kenji Hamaguchi https://orcid.org/0000-0001-7515-2779
Henrik Hartman https://orcid.org/0000-0001-9853-2555
Anthony F. J. Moffat https://orcid.org/0000-0002-4333-9755
Patrick Morris https://orcid.org/0000-0002-5186-4381
Krister Nielsen https://orcid.org/0000-0003-2636-7663
Julian M. Pittard https://orcid.org/0000-0003-2244-5070
Andrew M. T. Pollock https://orcid.org/0000-0002-5725-7072
Noel D. Richardson https://orcid.org/0000-0002-2806-9339
Ian R. Stevens https://orcid.org/0000-0001-7673-4340
Gerd Weigelt https://orcid.org/0000-0001-9754-2233

References

Corcoran, M. F., Hamaguchi, K., Pittard, J. M., et al. 2010, ApJ, 725, 1528
Corcoran, M. F., Liburd, J., Morris, D., et al. 2017, ApJ, 838, 45
Damineli, A. 1996, ApJL, 460, L49
Damineli, A., Conti, P. S., & Lopes, D. F. 1997, NewA, 2, 107
Damineli, A., Fernández-Lajús, E., Almeida, L. A., et al. 2019, MNRAS, 484, 1325
Damineli, A., Hillier, D. J., Corcoran, M. F., et al. 2008, MNRAS, 384, 1649
Damineli, A., Navarete, F., Hillier, D. J., et al. 2021, MNRAS, 505, 963

Damineli, A., Stahl, O., Kaufer, A., et al. 1998, A&AS, 133, 299
Davidson, K., Ishibashi, K., Martin, J. C., & Humphreys, R. M. 2018, ApJ, 858, 109
Espinoza Galeas, D., Corcoran, M. F., Hamaguchi, K., & Russell, C. 2021, AAS Meeting, 53, 204.10
Gaviola, E. 1950, ApJ, 111, 408
Grant, D., Blundell, K., & Matthews, J. 2020, MNRAS, 494, 17
Groh, J. H., Hillier, D. J., Madura, T. I., & Weigelt, G. 2012, MNRAS, 423, 3024
Groh, J. H., Nielsen, K. E., Damineli, A., et al. 2010, A&A, 517, A9
Gull, T. R., Kober, G. V., & Nielsen, K. E. 2006, ApJS, 163, 173
Gull, T. R., Madura, T. I., Groh, J. H., & Corcoran, M. F. 2011, ApJL, 743, L3
Gull, T. R., Madura, T. I., Teodoro, M., et al. 2016, MNRAS, 462, 3196
Gull, T. R., Nielsen, K. E., Corcoran, M. F., et al. 2009, MNRAS, 396, 1308
Herschel, J. F. W. 1838, MNRAS, 4, 121
Hillier, J. 2011, CMFGEN: Probing the Universe through Spectroscopy, Astrophysics Source Code Library, ascl:1109.020
Hirai, R., Podsiadlowski, P., Owocki, S. P., Schneider, F. R. N., & Smith, N. 2021, MNRAS, 503, 4276
Iping, R. C., Sonneborn, G., Gull, T. R., et al. 2005, ApJL, 633, L37
Ishibashi, K., Gull, T. R., Davidson, K., et al. 2003, AJ, 125, 3222
Madura, T. I. 2010, PhD thesis, Univ. Delaware
Madura, T. I., & Groh, J. H. 2012, ApJL, 746, L18
Madura, T. I., Gull, T. R., Okazaki, A. T., et al. 2013, MNRAS, 436, 3820
Madura, T. I., Gull, T. R., Owocki, S. P., et al. 2012, MNRAS, 420, 2064
Madura, T. I., & Owocki, S. P. 2010, RMxAC, 38, 52
Martin, J. C., Davidson, K., & Koppelman, M. D. 2006, AJ, 132, 2717
Martin, J. C., & Koppelman, M. D. 2004, AJ, 127, 2352
Mehner, A., Davidson, K., Ferland, G. J., & Humphreys, R. M. 2010, ApJ, 710, 729
Mehner, A., Davidson, K., Humphreys, R. M., et al. 2015, A&A, 578, A122
Mehner, A., de Wit, W. J., Asmus, D., et al. 2019, A&A, 630, L6
Morris, P. W., Gull, T. R., Hillier, D. J., et al. 2017, ApJ, 842, 79
Nielsen, K. E., Gull, T. R., & Vieira Kober, G. 2005, ApJS, 157, 138
Pittard, J. M., & Corcoran, M. F. 2002, A&A, 383, 636
Portegies Zwart, S. F., & van den Heuvel, E. P. J. 2016, MNRAS, 456, 3401
Richardson, N. D., Madura, T. I., St-Jean, L., et al. 2016, MNRAS, 461, 2540
Smith, N., & Frew, D. J. 2011, MNRAS, 415, 2009
Teodoro, M., Damineli, A., Heathcote, B., et al. 2016, ApJ, 819, 131
Valenti, J. A., Lindler, D., Bowers, C., Busko, I., & Quijano, J. K. 2002, Space Telescope STIS Instrument Science Report, STIS 2002-01
Viotti, R., & Rossi, C. 1999, MmSAI, 70, 503
Weigelt, G., Albrecht, R., Barbieri, C., et al. 1995, RMxAC, 2, 11
Weigelt, G., Hofmann, K.-H., Schertl, D., et al. 2021, A&A, 652, 140
Weigelt, G., Kraus, S., Driebe, T., et al. 2007, A&A, 464, 87